



저작자표시-비영리-변경금지 2.0 대한민국

이용자는 아래의 조건을 따르는 경우에 한하여 자유롭게

- 이 저작물을 복제, 배포, 전송, 전시, 공연 및 방송할 수 있습니다.

다음과 같은 조건을 따라야 합니다:



저작자표시. 귀하는 원저작자를 표시하여야 합니다.



비영리. 귀하는 이 저작물을 영리 목적으로 이용할 수 없습니다.



변경금지. 귀하는 이 저작물을 개작, 변형 또는 가공할 수 없습니다.

- 귀하는, 이 저작물의 재이용이나 배포의 경우, 이 저작물에 적용된 이용허락조건을 명확하게 나타내어야 합니다.
- 저작권자로부터 별도의 허가를 받으면 이러한 조건들은 적용되지 않습니다.

저작권법에 따른 이용자의 권리는 위의 내용에 의하여 영향을 받지 않습니다.

이것은 [이용허락규약\(Legal Code\)](#)을 이해하기 쉽게 요약한 것입니다.

[Disclaimer](#)

공학박사학위논문

**Efficient Generation of Strong Shock Waves
in Underwater Pulsed Spark Discharge**

수중 펄스 스파크 방전에서

강한 충격파의 효율적인 발생에 관한 연구

2015년 8월

서울대학교 대학원

에너지시스템공학부

이 석 근

Efficient Generation of Strong Shock Waves in Underwater Pulsed Spark Discharge

수중 펄스 스파크 방전에서
강한 충격파의 효율적인 발생에 관한 연구

지도교수 황 용 석

이 논문을 공학박사 학위논문으로 제출함
2015년 4월

서울대학교 대학원
에너지시스템학부
이 석 근

이석근의 공학박사 학위논문을 인준함
2015년 7월

위원장	<u>김 곤 호</u>	(印)
부위원장	<u>황 용 석</u>	(印)
위원	<u>고 광 철</u>	(印)
위원	<u>조 용 섭</u>	(印)
위원	<u>정 경 재</u>	(印)

Abstract

Efficient Generation of Strong Shock Waves in Underwater Pulsed Spark Discharge

Seok-geun Lee

Department of Energy System Engineering

The Graduate School

Seoul National University

There is considerable interest in the research of underwater pulsed discharge as a practical tool in environmental applications during the last two decades. Among the by-products generated by underwater pulsed discharge, shock wave is applied in various industrial fields. The numerous studies for increasing the strength of the shock wave have been researched because the application efficiency is higher with increasing the peak pressure. Therefore, this work investigates the mechanism of the shock wave formation in water and the effect of operating parameters on the peak pressure for finding the method of stronger shock wave formation using less energy.

The UPSD is consisted of two phase such as pre-breakdown phase and breakdown phase. The leakage energy during the pre-breakdown phase exists certainly and does not contribute to the spark channel expansion and shock wave formation after the breakdown. To reduce this leakage energy, it is effective that the energy for water heating, which occupy a large portion of the energy consumed for the pre-breakdown phase, decreases by changing the electrode geometry such as reducing the anode area. And the initial resistance of the spark channel is high as increasing the charging voltage at lower gap distance. It means that the

conductivity of the spark channel times channel cross section is a dominant factor rather than the length of the spark channel. To reduce the uncertainty, the experiments is carried out in the condition of narrow anode exposure area. Therefore, there will be no the leakage energy during the pre-breakdown phase.

The shock wave formation of water can be understood by the fundamental mechanism based on the shock wave generated by an accelerating piston. The shock wave is a result of the accumulation of the compression waves until the spark channel expansion speed reaches the maximum value of the speed. Therefore, the delivered energy to the spark channel during the accelerating phase of the spark channel is a critical parameter to determine the peak pressure. To compute this energy, it is needed the time of maximum channel expansion speed obtained from the modified power balance equation. When the power is integrated over time of maximum channel expansion speed, the delivered energy to the spark channel during the acceleration phase (E^*) is obtained. As a result of the experiments, the strength of the shock wave pressure measured at a specific position sufficiently far from the spark channel is proportional to E^* .

The resistance of the spark channel is important to determine the E^* . Therefore, E^* of the experiment compares with E^* calculated by using channel resistance models. As a result, the channel resistance is not a constant value but time-varying waveform. As decreasing the channel resistance rapidly, calculated E^* shows the low value.

The shock wave formed by an underwater spark discharge is a highly transient and nonlinear phenomenon. The spark channel resistance and the delivered power to the spark channel mutually interact. For this reason, the self-consistent model is constructed. By using this model, the optimum condition of the strong shock wave formation is investigated.

To generate the strong shock wave, it is important to increase the energy absorbed to the spark channel at early stage of the discharge. It is possible that this

energy is adjusted effectively by selecting the appropriate operating parameters such as the capacitance, breakdown voltage and gap distance. As increasing the capacitance with fixed breakdown voltage and gap distance, the peak pressure and E^* tends to saturate above specific capacitance. In case of variable breakdown voltage with fixed capacitance and gap distance, the peak pressure and E^* increase with increasing the breakdown voltage because the power rising rate is faster with higher breakdown voltage while t^* is saturated. Finally, the longer gap distance make the strong peak pressure at the fixed capacitance and the breakdown voltage, because the long gap distance make the initial resistance of the spark channel is high and it leads to increase the rising rate of the power, although the problem of the increasing breakdown voltage with increasing the gap distance.

This research provides the better understanding of the shock wave formation mechanism and the fundamental operating parameters for obtaining the strong shock wave.

Keywords: Underwater pulsed spark discharge (UPSD), Shock wave, Peak pressure, Maximum channel expansion speed, Energy absorbed during the acceleration phase, Spark channel resistance

Student number: 2008-30897

Name in English: Seok-geun Lee

Table of Contents

Abstract	i
Table of Contents	iv
List of Figures	vi
List of Tables	xi
Chapter 1 Introduction	1
1.1 Underwater Pulsed Spark Discharge (UPSD).....	1
1.2 Applications of UPSD Technique.....	6
1.2.1 Ballast Water Treatment Applications.....	6
1.2.2 Well Rehabilitation Applications.....	10
1.3 Previous Work and Research Motivation.....	12
1.3.1 Previous Work	12
1.3.2 Research Motivation and Scope of the Research	17
Chapter 2 Experimental Setup and Diagnostics	19
2.1 Experimental Setup	19
2.1.1 High-Voltage Pulsed Power System.....	21
2.1.2 Discharge Electrode	23
2.2 Diagnostics of Electrical Characteristics and Pressure	25
Chapter 3 Pre-breakdown Process	30
3.1 Bubble formation and Streamer Discharge in Bubble	30
3.2 Energy Consumption during Pre-breakdown.....	34
3.3 Initial resistance of the spark channel.....	38
Chapter 4 Mechanism of the Shock Wave Formation	41
4.1 Shock Wave Formation by an Expanding Spark Channel	41
4.2 1D Model for Spark Channel Expansion	47
4.3 Relationship between Peak Pressure and E^*	53
Chapter 5 Analysis for Efficient Generation of Strong Shock Waves	58

5.1	Energy Efficiency for Shock Wave Formation.....	58
5.2	Effect of Initial Resistance of Spark Channel.....	61
5.3	Correlation of Spark Channel Resistance and E^*	63
5.3.1	Effects of Spark Channel Resistance on E^*	63
5.3.2	Limitation of Resistance Model	69
5.3.3	1D MHD Model	71
5.4	Effects of Operating parameters on Peak Pressure.....	76
5.4.1	Effect of Capacitance.....	76
5.4.2	Effect of Breakdown Voltage	78
5.4.3	Effect of Gap Distance	81
Chapter 6	Conclusion	82
References	84
Abstract in Korean	88

List of Figures

Figure 1.1	The by-products generated by underwater pulsed spark discharge	1
Figure 1.2	Images of the bubble development at the pin anode before the breakdown.	3
Figure 1.3	Shadowgraph images (a, b) of non-luminous streamers emanating from a pin cathode into water with a rectangular voltage pulse of 200 ns (full width half maximum). Shutter images (c, d) of a single luminous streamer across the gap with application of a positive voltage pulse.....	4
Figure 1.4	Schematic diagram of the comparison of streamer, spark and arc discharge.....	5
Figure 1.5	The effect of the shock wave treatment on the zooplankton cell destruction with the neutral red dyeing method (red dyeing cell: live, green dyeing cell: dead)	8
Figure 1.6	Comparison of the live zooplankton cell's population with various peak pressure.....	9
Figure 1.7	Comparison of the well screen condition before and after underwater shock wave cleaning treatment in field test	11
Figure 1.8	Comparison of the removal amount of the oil-based paint from the screen depending on the charging voltage (peak pressure amplitude) in preliminary experiment (a) the effect of the low peak pressure (charging voltage: 3.7 kV) on the removal of the paint, (b) the effect of the high peak pressure (charging voltage: 4.2 kV) on the removal of the paint	12
Figure 1.9	Peak pressure versus peak current for various experimental conditions. ...	13
Figure 1.10	Peak pressure as a function of the product breakdown voltage and peak current.....	14
Figure 1.11	Variation of peak pressure with energy at breakdown time for three distances between the sensor and the discharge.....	15

Figure 1.12	Plot of peak pinducer response against the pulse energy at breakdown. Blank circle means the peak pinducer response.....	16
Figure 1.13	Acoustic signals and calculated peak pressure response produced by underwater discharges as a function of energy	17
Figure 2.1	Schematic diagram of experimental apparatus to generate spark channel with monitoring tools such as high voltage probe, current probe, pressure sensor and fast camera.....	20
Figure 2.2	(a) Equivalent circuit diagram of high-voltage pulsed power pulsed system, (b) photograph of the high-voltage pulsed power system.....	22
Figure 2.3	(a) The damaged cylindrical shape electrode after the breakdown, (b) the improved electrode with dome type structure	23
Figure 2.4	Schematic diagram of the improved electrodes at side cross-sectional view with rubber O-ring.....	24
Figure 2.5	Experimental results of short-circuit test: (a) measured voltage difference and current in short-circuit test with the capacitance of 5.22 μF and the charging voltage of 4 kV, (b) comparison of the current waveform in experiment and simulation.....	26
Figure 2.6	Typical waveforms of the gap voltage (V_g), resistive voltage (V_r), current and pressure. The resistive voltage is obtained by subtraction inductive voltage term from the measured gap voltage across the electrode	28
Figure 2.7	The pressure amplitudes is measured at intervals of 10 mm. The pressure amplitude decreases inversely as the distance from the axis of the spark channel, irrespective of measurement angle. Determination of the measurement angle based on the axis of the spark channel at top view	29
Figure 2.8	Propagation of the pressure wave with the sound velocity.....	29
Figure 3.1	Typical waveform of the voltage and the current in UPSD with capacitance of 1 μF , gap distance of 6 mm and charging voltage of 20 kV	30

Figure 3.2	(a) corresponding raw images of the bubble generation with a back light, and (b) converted color images of the streamer evolution without back light during the pre-breakdown phase taken by fast CCD camera.....	31
Figure 3.3	Typical waveform of the voltage and the current in UPSD with capacitance of 1 μ F, gap distance of 6 mm and charging voltage of 20 kV	32
Figure 3.4	Typical waveform of the voltage and the current in UPSD with capacitance of 1 μ F, gap distance of 6 mm and charging voltage of 20 kV	34
Figure 3.5	Energy consumed for the each stage of the pre-breakdown phase with various charging voltage and gap distance	36
Figure 3.6	Comparison of the energy consumption for the pre-breakdown phase versus charging voltage and anode area with capacitance of 1 μ F and gap distance of 5 mm. (anode area ■: 9π mm ² , ●: 18π mm ²).....	37
Figure 3.7	Comparison of the bubble size as varying charging voltage with capacitance of 1 μ F and gap distance of 7 mm	39
Figure 3.8	Plot of the resistance of water gap versus the charging voltage during the pre-breakdown phase with capacitance 1 μ F and gap distance 7 mm	40
Figure 4.1	Schematic diagram of the mechanism of the shock wave formation by an accelerating piston in fluids	42
Figure 4.2	Schematic diagram of the generation of the compression waves by an expanding spark channel	43
Figure 4.3	Schematic diagram of the generation of the compression waves by an expanding spark channel	44
Figure 4.4	(a) Schematic diagram of the accumulation of the compression waves for the time of maximum spark channel expansion speed, (b) the time-distance graph of two compression wave at $t = 0$ and $t = t^*$	46
Figure 4.5	Schematic diagram of the distribution of the pressure under the shock wave formation	47

Figure 4.6	Schematic diagram of density, velocity and pressure of two regime across the shock front	48
Figure 4.7	(a) The gap voltage (V_g), resistive voltage (V_r) and current waveforms for the charging voltage of 14 kV with a capacitance of 5.22 μ F, (b) the Joule heating power ($P(t) = V_r(t) \times i(t)$), (c) the spark channel expansion speed derived from the power balance model, and (d) the absorbed energy in the spark channel until t^* , where t^* is the time required for the channel expansion speed to reach its maximum	52
Figure 4.8	Dependency of the peak pressure measured at 100 mm from the axis of the spark channel on the remaining energy stored in the capacitor at breakdown (E_b) with various charging voltage and capacitance	54
Figure 4.9	Dependency of the peak pressure measured at 100 mm from the axis of the spark channel on the energy absorption in the spark channel until the spark channel expansion speed reaches its maximum value (E^*) with various charging voltage and capacitance	55
Figure 4.10	Comparison of the current, power, channel expansion speed and energy absorption in the spark channel (E^*) in two different experimental conditions with similar peak pressures (A: $C_0 = 5.22 \mu$ F, $V_b = 13.11$ kV; B: $C_0 = 1 \mu$ F, $V_b = 16.18$ kV). The calculated value of E^* for the two cases are similar to be ~ 6 J	57
Figure 5.1	Typical waveforms of voltage and current: (a) full scale, (b) specific scale after the breakdown	58
Figure 5.2	Energy efficiency for shock wave formation with considering the mechanism of the shock wave formation	59
Figure 5.3	Comparison of the breakdown voltage and initial resistance of the spark channel with various charging voltages and gap distances under the capacitance of 1 μ F	61

Figure 5.4	Comparison of the peak pressure as increasing $V_b^2 \times R_0$ with various gap distances and the fixed capacitance of 1 μF	63
Figure 5.5	(a) Arbitrary current waveform obtained from equation (5.6), (b) Comparison of the power waveform depending on the resistance model with identical arbitrary current waveform of (a)	67
Figure 5.6	Comparison of the energy absorbed in the spark channel until the channel expansion speed reaches the maximum value between experiment and the resistance models with changing the capacitance.....	68
Figure 5.7	Comparison of the power waveform between experiment and the resistance model with capacitance of 5.22 μF , maximum power of 8MW	69
Figure 5.8	Comparison of the resistance between experiment and various resistance model with capacitance of 5.22 μF , maximum power of 8MW	70
Figure 5.9	Electrical conductivities of water plasma with temperature and mass density ratio ($\delta = \text{plasma density/water density at STP}$).....	71
Figure 5.10	Equivalent circuit of the UPSD system	72
Figure 5.11	Comparison of (a) the voltage, current, and pressure waveforms (b) the calculated spark channel resistance between experiment and simulation with the charging voltage of 14 kV	75
Figure 5.12	Comparison of the E^* and peak pressure versus various capacitance in identical charging voltage of 14 kV.....	76
Figure 5.13	Comparison of the power waveforms until t^* with various capacitance ...	77
Figure 5.14	Comparison of the peak pressure with changing the breakdown voltage and gap distance in identical capacitance.....	78
Figure 5.15	Comparison of E^* and t^* with various maximum power (breakdown voltage) in identical capacitance.....	80
Figure 5.16	Comparison of E^* with two gap distance and various capacitances at the fixed breakdown voltage of 20 kV	81

List of Tables

Table 1.1	The characteristics of the developed ballast water treatment techniques	7
Table 2.1	Electrical parameters of the pulsed system in the short circuit test	27
Table 5.1	Comparison of the resistance models of the spark channel	65

Chapter 1 Introduction

1.1 Underwater Pulsed Spark Discharge (UPSD)

Electrical breakdown of water occurs in the gap, when high-voltage is applied between two adjacent electrodes immersed in water. The breakdown forms an electrically conducting plasma channel in the water gap, and simultaneously UV radiation, active radicals (OH, O, H₂O₂, etc) and shock waves as shown in Figure 1.1[1]. These accompanying by-products are effective to decontaminate or sterilize polluted water. For this reason, the electrical discharge in water draws attention as a practical tool in environmental applications during the last two decades [2].

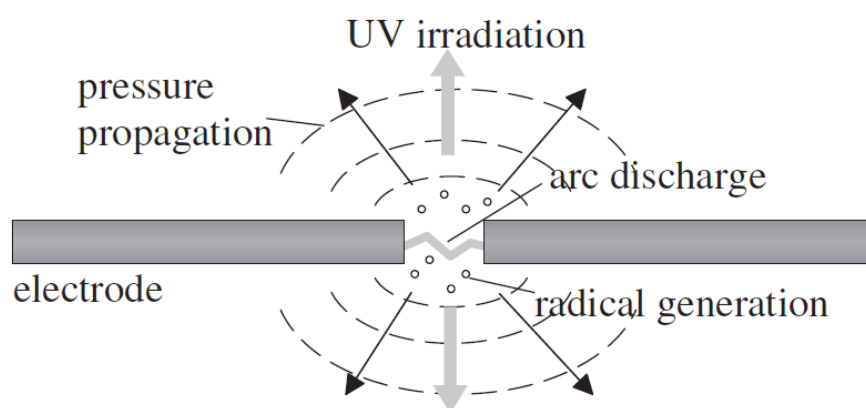


Figure 1.1 The by-products generated by underwater pulsed spark discharge [1].

Among the by-products generated by UPSD, shock waves have the merit of deep penetration in comparison with others. Because of the characteristics of the underwater shock waves to propagate far away from the spark source, shock wave applications become more extensive. Several researches for the application of shock wave have been already developed in the fields of sound source [3, 4], extracorporeal shock wave lithotripsy [5] and cleaning the well [6]. For more efficient applications, it is necessary to understand the mechanism of the electrical discharge in water and the process of the shock waves formation by an expanding spark channel in the electrical discharge.

The mechanism of the electrical discharge in liquids is more complicated than in gases or solids, because the density of liquids is much higher than that of gases and the mean free path of liquids is not the long range order seen in solids [2, 7]. Additionally, the dissolved gases and impurities in water, which form the micro bubbles, make it more complicated to comprehend the process of electrical discharge in water.

Two kinds of thoughts in respect of breakdown initiation in liquids have been appeared in history. The first thought is based on electron avalanche directly in the liquid, whereas the second thought is based on the mechanism of a bubble formation (or a phase change) before breakdown [7]. The former relies on electron avalanche to initiate breakdown. However, electron avalanche processes in bulk water may be almost impossible. Liquids are so much denser than gases that the scattering rates are high and the mean-free paths are low. This facts leads to very low probabilities for the electron to reach the requisite ionization energy thresholds. Additionally, free electrons are generally absent in water because they are quickly solvated within 1 ps time scales [8]. The concept of the bubble mechanism, on the other hand, make it possible to electron multiplication by creating a locally low-density regime(see Figure 1.2).

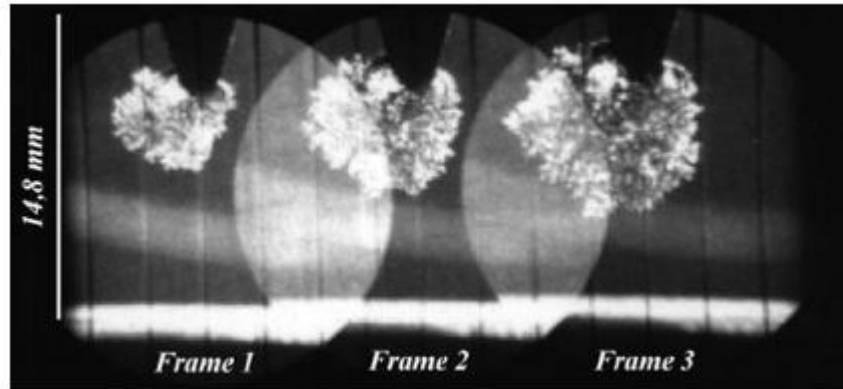


Figure 1.2 Images of the bubble development at the pin anode before the breakdown [9].

Generally, the underwater electrical breakdown is defined as the formation of the conducting plasma channel which connects electrically between two metal electrodes in the liquid. The time delay in breakdown after applying high voltage to the electrode is always observed in the underwater electrical discharge. If the time delay is longer than the order of approximately microsecond, the bubble formation is observed at the high voltage electrode and the streamer discharge occurs in the bubble during this time delay named as pre-breakdown. The generated streamer propagates to the other electrode as shown in Figure 1.3 and it leads to transition from the streamer to the spark channel [10].

The underwater electrical discharges can be classified by the plasma channel formation as shown in Figure 1.4 [11]. If a streamer does not reach the opposite electrode, it is called a corona discharge. Whereas, if a streamer reaches the opposite electrode, the plasma channel, which connects electrically between two metal electrodes, is formed. If the transient current flows through the plasma channel, it is called a spark discharge. If the current flows continuously through the plasma channel, it is usually called an arc discharge [12].

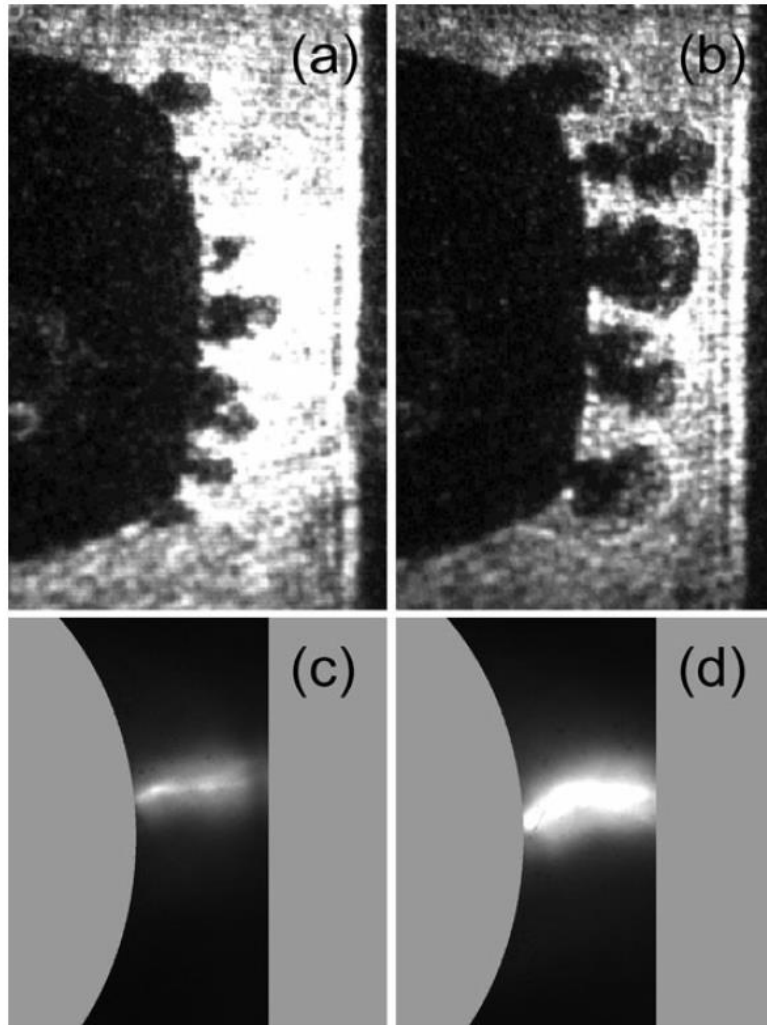


Figure 1.3 Shadowgraph images (a, b) of non-luminous streamers emanating from a pin cathode into water with a rectangular voltage pulse of 200 ns (full width half maximum). Shutter images (c, d) of a single luminous streamer across the gap with application of a positive voltage pulse [10].

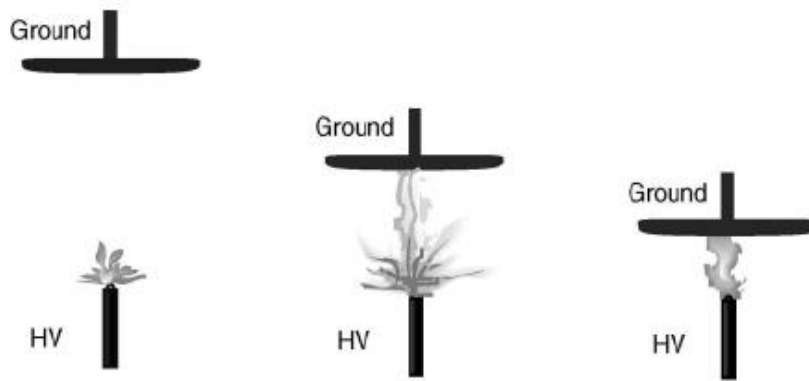


Figure 1.4 Schematic diagram of the comparison of streamer, spark and arc discharge [11].

In the corona discharge the current is transferred by slow ions. In case of water with a high electrical conductivity, a large discharge current flows, resulting in a shortening of the streamer length due to the faster compensation of the space charge electric fields on the head of streamers. Subsequently, a higher power density, i.e., a higher plasma density, in the channel can be obtained, resulting in a higher plasma temperature, a higher UV radiation, and the generation of acoustic waves.

In the arc or spark discharges, the current is transferred by electrons. The high current heats a small volume of plasma in the gap between two electrodes, generating quasi-thermal plasma, where the temperatures of electrons and heavy particles are almost equal. When a high-voltage, high-current discharge takes place between two submerged electrodes, a large part of the energy is consumed in the formation of a thermal plasma channel. This channel emits UV radiation, and its expansion against the surrounding water generates intense shockwaves. The shockwave can directly interact with the microorganisms in water. In case of the underwater corona discharge, the shockwaves are weak or moderate, whereas the shockwaves are generally very strong in case of the underwater pulsed arc or

spark discharge [12].

1.2 Applications of UPSD Technique

As stated above, the shock wave generated by UPSD are useful to the various industrial fields. The strong shock wave has an opportunity to become more extensive industrial fields besides the purification of polluted water. This section introduces the two applications of the shock wave.

1.2.1 Ballast Water Treatment Applications

The ballast water, which is loaded in the vessel for the stability of the vessel, is an international negative issue with respect to the marine environment. The ballast water is taken from coastal port areas for unloading cargo and expelled to the faraway next port for loading cargo. The ballast water, which move long distances, contains various marine organism such as plant, marine animals, plankton, microbes, bacteria, small invertebrates, eggs, cysts and larvae of various species. These invasive species can cause negative effect to native aquatic ecosystems. There are numerous reports with respect to the damage by invasive species all over the world, since the first report of the damage by invasive species in Great Lakes, Canada was announced in 1988. The Marine Environment Protection Committee (MPEC) of the International Maritime Organization (IMO) adopted guidelines for ballast water management in 1997 and required all of the vessels to implement a ballast water management plan [13].

There were considerable efforts to formulate appropriate standards for ballast water management. They are the ballast water exchange standard and the

ballast water performance standard. Ships performing ballast water exchange shall do so with an efficiency of 95 percent volumetric exchange of ballast water and ships using a ballast water management system shall meet a performance standard based on agreed numbers of organisms per unit of volume. In this situation, there are numerous research for ballast water treatment system to meet the standard condition [13].

The developed ballast water treatment techniques are summarized in Table 1.1 [14]. The techniques using a chemical reactions are very efficient for the ballast water treatment, but are possible to occur the second contamination. Whereas the techniques using a physical effect are safe to environment, but have a weakness of the low treatment efficiency.

Table 1.1 Characteristics of the developed ballast water treatment techniques [14].

Treatment Technique	Features	Weakness
UV radiation	Safety	Low efficiency
Ozone	Safety	2 nd contamination High cost
Sodium hypochlorite (NaOCl)	No 2 nd contamination Not toxic	Danger of high concentration water to marine creature Corrosion
Filter	Treatment and water inflow in parallel	Difficulty in removing fine organism
Heat treatment	Long operation at 36~38 °C	Continuous management Low efficiency to microorganism
chlorine dioxide(ClO ₂)	High efficiency	2 nd contamination

To develop the innovative ballast water treatment technique, the application of the shock wave generated by UPSD is researched. The technique using the underwater shock wave does not cause the second contamination. Furthermore, it is expected that the treatment efficiency is high, because the shock wave propagate quickly and deeply throughout water in a short time. In other words, the ballast water treatment technique using underwater shock wave supplements the weakness of the existing techniques with chemical reactions and physical effects.

Figure 1.4 shows the effectiveness of the underwater shock wave to destruct the zooplankton cell. The population of the live and dead zooplankton cell before and after underwater shock wave treatment are compared by the neutral red dyeing method. The red dyeing cell means live cell and the green dyeing cell means dead cell. As a result, the population of the zooplankton decreases definitely after underwater shock wave treatment [15].

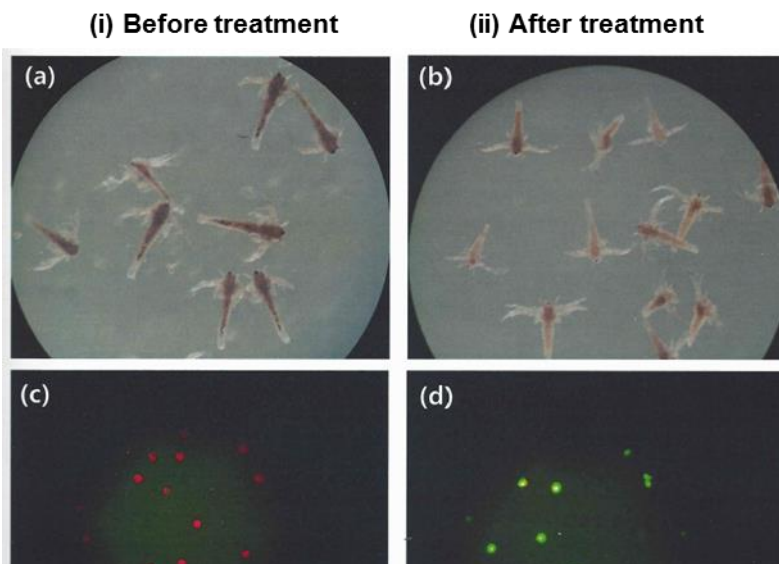
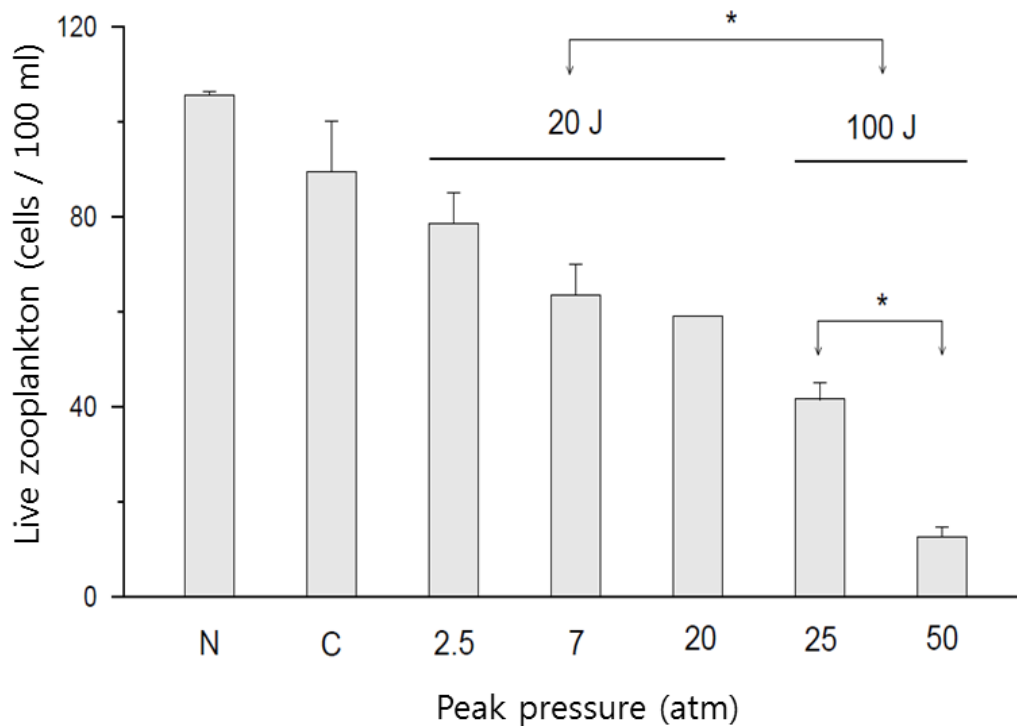


Figure 1.5 The effect of the shock wave treatment on the zooplankton cell destruction with the neutral red dyeing method (red dyeing cell: live, green dyeing cell: dead) [15].

The comparison result of the live zooplankton cell's population per volume of 100 ml with the various peak pressure is shown in Figure 1.5. All of the experiments are carried out under water circulation. 'N' and 'C' in the Figure 1.5 mean an initial sample condition and a control sample (only water circulation) without discharge, respectively. This diagram conclude that live zooplankton cell's population decrease with increasing the peak pressure. Especially, the treatment efficiency of the zooplankton is higher with the higher peak pressure under the identical stored energy in the capacitor [16].



N: samples without discharge and circulation.
 C: control samples with circulation (no discharge)
 Others: 500 times discharge

Figure 1.6 Comparison of the live zooplankton cell's population with various peak pressure.

1.2.2 Well Rehabilitation Applications

As time passed, the clogging material blocks the screen of the well. Consequently, the groundwater yield decreases due to clogging of the well. The application of the appropriate rehabilitation techniques can improve the efficiency of the clogged well and extend their life. There are several conventional cleaning techniques by using a mechanical and chemical means for well rehabilitation. Above all, the mechanical cleaning techniques include wire brushing/scraping, blasting and gas pressure jet. The methods of blasting or gas pressure jet utilize the strong pressure (or shock) generated by an explosive or a compressed fluid. However, the blasting cleaning technique poses a risk of exploding due to the explosive and has a difficulty of complicated process of the cleaning. And the gas jet cleaning technique needs the bulk and high purity nitrogen gas. Whereas, the well cleaning technique using high-voltage pulsed discharge, in which electrical energy is used to produce impulsive pressure in water, supplements this weakness of those cleaning techniques using a pressure generated by an explosive or a compressed gas. Compared with conventional techniques, the well cleaning technique using high-voltage pulsed discharge is simple, and easy to handle and control [17].

Figure 1.6 shows the comparison of the well screen before and after the treatment with the cleaning technique using high-voltage pulsed discharge. It is assured that the clogged materials are almost removed from the screen of the well and the well cleaning technique using high-voltage pulsed discharge is useful to rehabilitate the clogged well. To investigate the effect of the strength of the peak pressure on the efficiency of the cleaning, the preliminary experiment carried out in a laboratory. Figure 1.7 shows the qualitative analysis results of preliminary experiment. The removal rate of the relatively lower pressure (low charging voltage: 3.7 kV) is roughly 50 %. On the other hand, the removal rate of the

relatively higher pressure (high charging voltage: 4.2 kV) is almost 100 %. It is concluded that the efficiency of the well cleaning is improved with increasing the strength of the peak pressure.

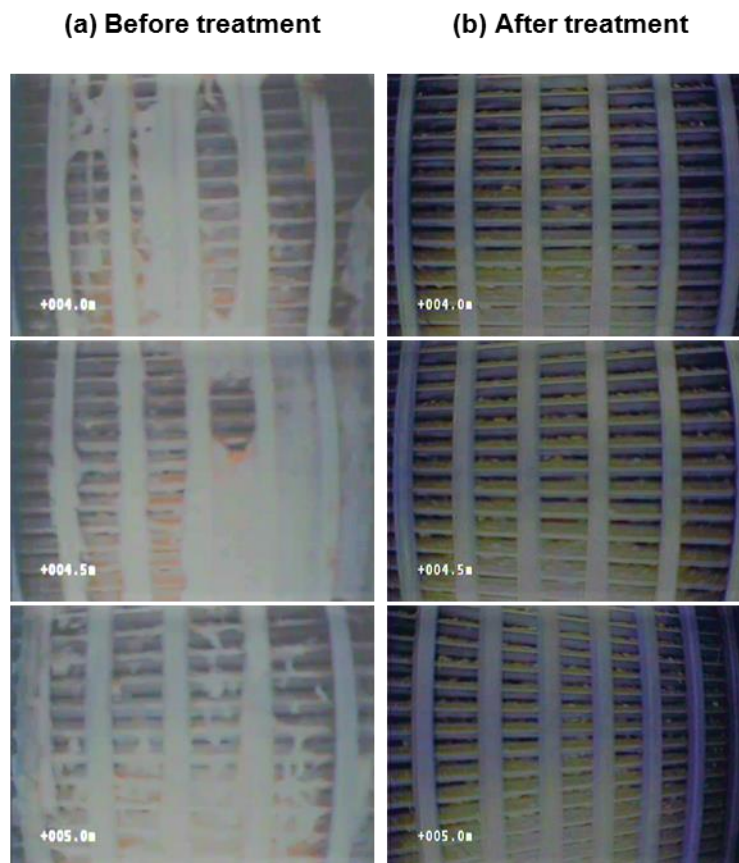


Figure 1.7 Comparison of the well screen condition before and after underwater shock wave cleaning treatment in field test [6].

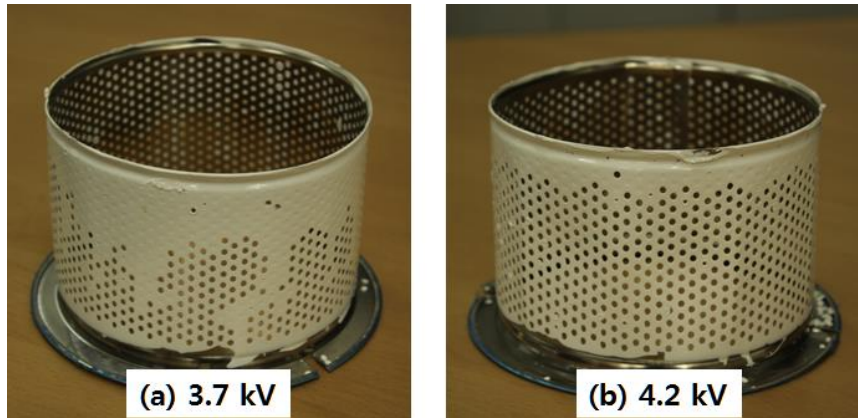


Figure 1.8 Comparison of the removal amount of the oil-based paint from the screen depending on the charging voltage (peak pressure amplitude) in preliminary experiment (a) the effect of the low peak pressure (charging voltage: 3.7 kV) on the removal of the paint, (b) the effect of the high peak pressure (charging voltage: 4.2 kV) on the removal of the paint.

1.3 Previous Work and Research Motivation

1.3.1 Previous Work

As described in previous section, the treatment efficiency of the underwater shock wave is generally proportional to the strength of the peak pressure. Therefore, the method for obtaining a strong peak pressure while minimizing the equipment size and the applied energy should be investigate for the development of an efficient underwater shock wave system.

As stated above, when a sufficiently high voltage is applied to a small gap between two adjacent electrodes immersed in water, electrical breakdown occurs water in the gap, forming an electrically conducting plasma channel. Formation of

the conducting plasma channel is immediately followed by rapid Joule heating of the channel provided by an external circuit. The heated spark channel expands rapidly and compresses the surrounding water, resulting in the development of a shock wave of over GPa in water [18]. The generated shock wave is separated from the spark channel after a while and propagates in the radial direction with a speed faster than the sound speed in water, depending on the strength of the shock wave. This underwater shock wave propagates far away from the spark source and is utilized for various applications mentioned above.

Until now, most researchers have estimated the peak pressure generated by an underwater spark discharge differently by using apparent parameters such as the capacitor voltage at breakdown and the peak current during the discharge. In early experiments for the generation of acoustic pressure by using a spark discharge, Caulfield [19] reported that the peak pressure was linearly proportional

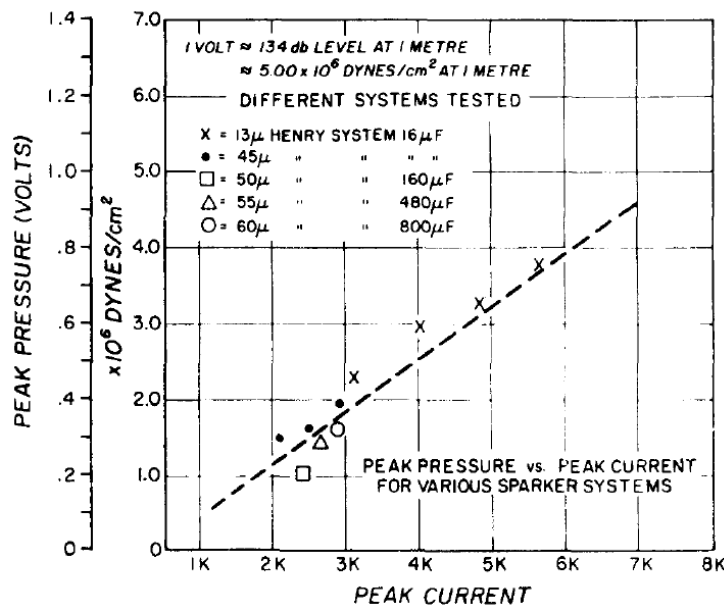


Figure 1.9 Peak pressure versus peak current for various experimental conditions [19].

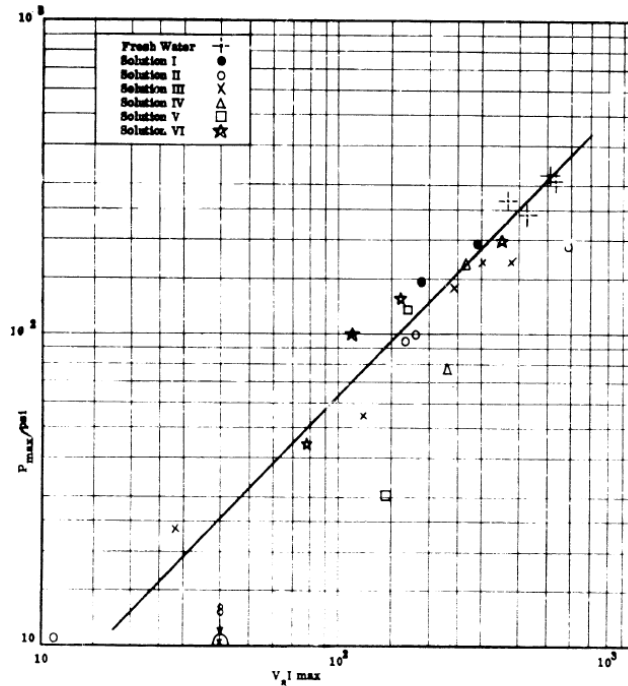


Figure 37. Peak Acoustic Pressure as a Function of the Product (Voltage at Arc) x (Peak Current)

Figure 1.10 Peak pressure as a function of the product breakdown voltage and peak current [20].

to the peak current irrespective of circuit inductance as well as the capacitance of the energy storage capacitor. However, a few years later, Guman and Humphrey [19] reported a quite different experimental result; the peak pressure was linearly proportional to the product of breakdown voltage and peak current rather than to peak current alone. The product of breakdown voltage and peak current is noted to correspond to the energy stored in the capacitor at the time of breakdown, since the peak current is linearly proportional to the breakdown voltage at the given circuit parameters. Recent experiments carried out by Touya *et al.* [9] also reported that the peak pressure as a function of the energy stored in the capacitor at breakdown as shown in Figure 1.10. Such a nonlinear dependency of the peak

pressure on the energy stored in the capacitor at breakdown was also observed by Mackersie *et al.* [21]. From numerous experiments with various values of the

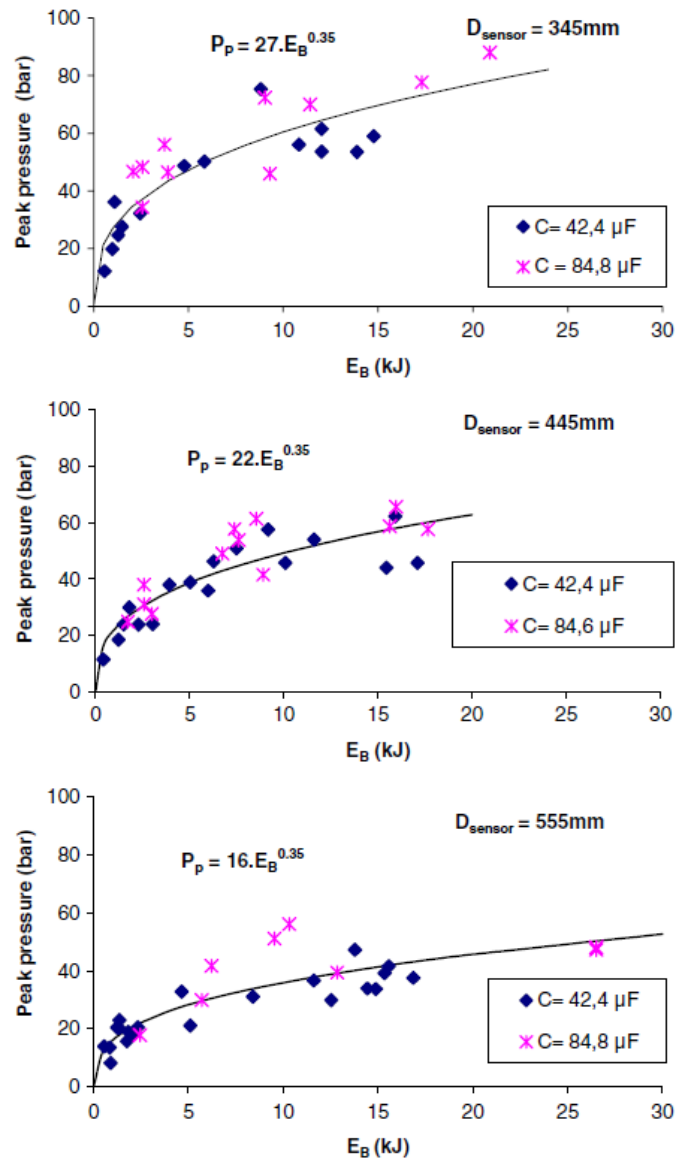


Figure 1.11 Variation of peak pressure with energy at breakdown time for three distances between the sensor and the discharge [9].

stored energy in the capacitor at breakdown, they found that the peak pressure rose sharply for the stored energy of up to ~ 25 J and then saturated, indicating little gain by increasing the stored energy indefinitely as shown in Figure 1.11. Using a zero-dimensional hydrodynamic model coupled to the capacitive circuit equation, Timoshkin *et al.* [22] could explain their experimental results in a phenomenological way. As shown in Figure 1.12, they also found that increasing breakdown voltage was better than increasing capacitance for obtaining a stronger shock wave with the same energy stored in the capacitor at breakdown, which is different from the experimental observation made by Touya *et al.* [9].

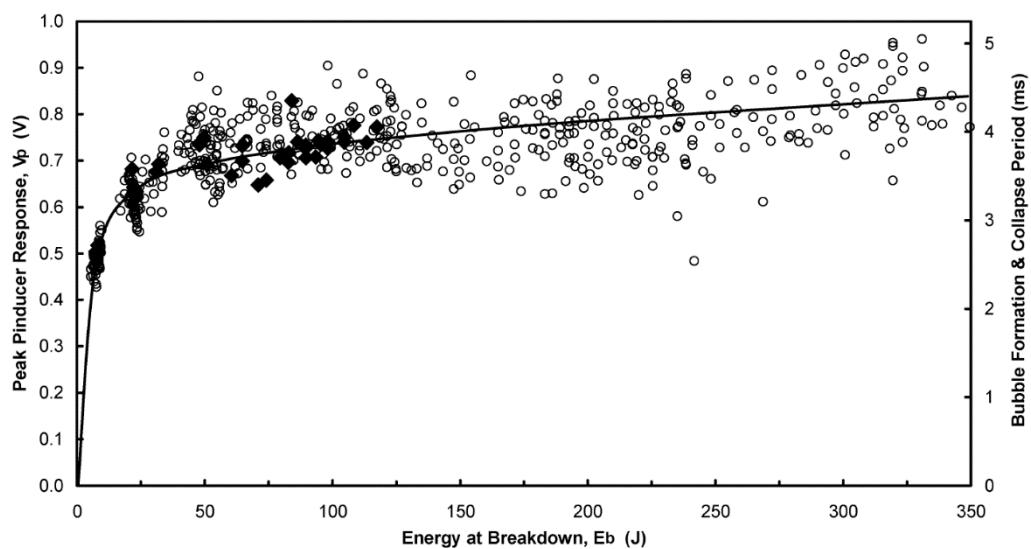


Figure 1.12 Plot of peak pinducer response against the pulse energy at breakdown. Blank circle means the peak pinducer response [21].

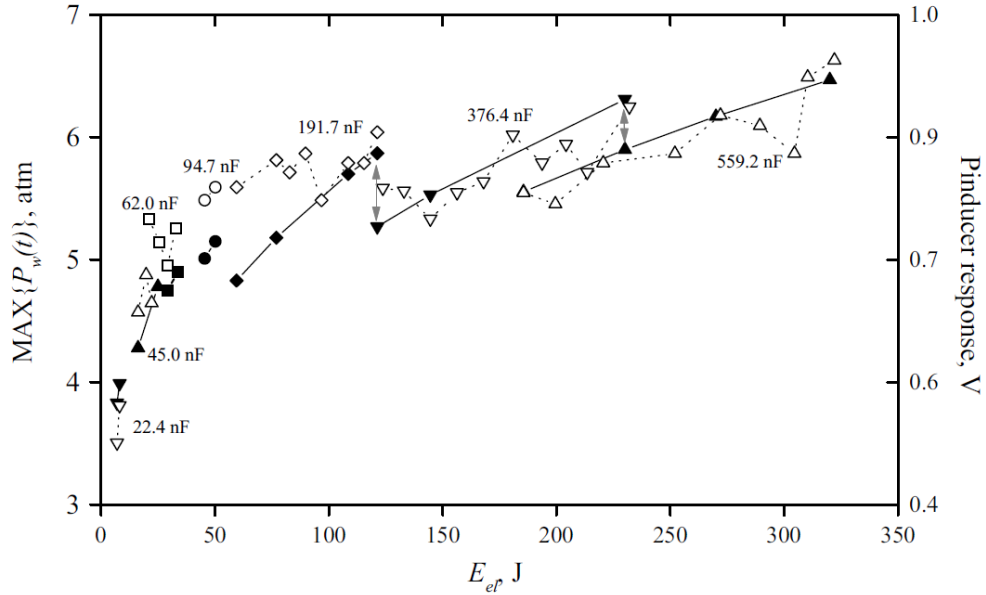


Figure 1.13 Acoustic signals and calculated peak pressure response produced by underwater discharges as a function of energy [22].

1.3.2 Research Motivation and Scope of the Research

The shock wave generated by underwater pulsed spark discharge has a high potential for the application in various fields. There were numerous researches to find the key factor affecting the strength of the shock pressure during the past century. Figure 1.11 shows the dependency of the peak pressure on the stored energy in the capacitor at breakdown irrespective of the capacitance. However, Figure 1.13 shows that the breakdown with higher voltage (lower capacitance) generates stronger peak pressure for an identical energy stored in the capacitor at breakdown. The present research is motivated by the fact that the proposed factor for higher peak pressure is not consistent with each other as stated above. It is recognized that the inconsistency might be caused by ignorance of the transient

process of shock wave formation occurring immediately after the onset of a spark discharge [9, 21, 22]. The generated shock pressure by an underwater spark discharge is a highly transient and nonlinear phenomenon in which the radial acceleration of the spark channel by external heating compresses the adjacent water layer and generates a strong shock wave in the water [18]. Nevertheless, its fundamental mechanism can be easily understood with an analogy to the shock wave generated by an accelerating piston [24]. Compression waves generated by an accelerating piston are known to move faster than the speed of sound so that they overtake the initial disturbance wave and intensify it. Therefore, in this dissertation, we attempt to explain the correlation of the amplitude of the underwater shock pressure with the energy absorbed during the accelerating phase of the spark channel which only contributes to the formation of the peak pressure.

This dissertation is organized as follows. Chapter 2 is account for the experimental setup and diagnostic tools. In Chap. 3, the process of the pre-breakdown will be described. And the correlation between the pre-breakdown process and the initial condition of the spark channel at breakdown will be explained at the end of Chap. 3. The principle of the shock wave formation after breakdown in underwater discharge will be introduced in the Chap. 4. As based on the result in Chap. 4, Chap. 5 is devoted to the correlation between the peak pressure and the energy absorbed in the spark channel at early stage of discharge. Chapter 6 will present summary and conclusion of this research.

Chapter 2 Experimental Setup and Diagnostics

2.1 Experimental Setup

Figure 2.1 shows a schematic diagram of the experimental setup, which is composed of a cylindrical discharge chamber, a pulsed power system, and various diagnostic tools. The cylindrical discharge chamber is made by stainless steel and the equipment of the inlet and the outlet is installed in the discharge chamber for water circulation. The four Quartz windows is installed in the discharge chamber for observing the spark channel. And the insulator adaptor, which is colored as green in Figure 2.1, is installed at the position of electrode installation for high voltage insulation. The rod-rod electrode system is located in the middle of the discharge chamber with a volume of 11 liters filled with tap water. The electrodes are made of tungsten, and their tips are rounded to prevent them from being damaged by high current arcs and thus improve their lifetime. The anode with a diameter of 3 mm is located at the bottom of the chamber, and the cathode with a diameter of 6 mm is located at the opposite position. The gap distance between two electrodes is variable from 5 mm to 10 mm by inserting 1 mm insulator adaptor.

A pulsed high-voltage is applied to the electrodes by using a capacitive pulsed power system. The energy-storage capacitor is charged by using a high-voltage DC power supply (Glassman, WX75R12) and discharges to the water gap through a mechanical switch operating pneumatically. In the experiments, three capacitance values, 1.00, 5.22, and 10.37 μF , are utilized to control the amount of

energy in the capacitor at the time of breakdown. For example, the capacitor with a capacitance of $10.37 \mu\text{F}$ has an energy of 1,327 J at breakdown voltage = 16 kV, while the capacitor with a capacitance of $1 \mu\text{F}$ only has an energy of 128 J at the same breakdown voltage. This allows us to conduct the experiments with various energy ranges depending on the combination of capacitance and voltage.

The voltage and current across the gap are measured with two high-voltage probes (Tektronix, P6015A) and current transformer (Pearson Electronics Inc., 301X), respectively. The shock pressure is measured with a piezoelectric sensor (PCB Piezotronics, S113B23) located 100 mm away from the center of the discharge. The pressure sensor can measure the maximum value approximately 70 MPa. The spark channel is monitored and recorded by a fast CCD camera (NAC Inc., Memrecam GX-8). The maximum frame rate of a fast CCD camera is

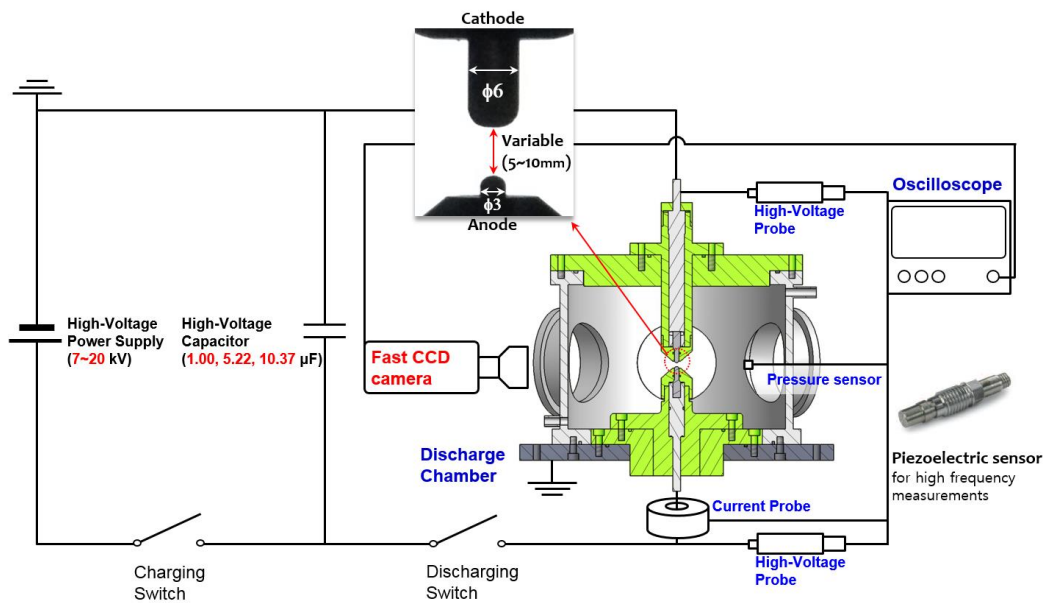


Figure 2.1 Schematic diagram of experimental apparatus to generate spark channel with monitoring tools such as high voltage probe, current probe, pressure sensor and fast camera.

600,000 fps. In this experiment, the accepted frame rate, exposure time and frame size are 100,000 fps, 1 μ s and 144x108 pixels respectively in order to record the phenomenon for the pre-breakdown process. And a fast CCD camera is triggered by an output signal of the oscilloscope matched with the voltage signal of anode.

2.1.1 High-Voltage Pulsed Power System

The capacitive high-voltage pulsed power system which have the characteristics of simple structure, low cost and good durability is accepted in this experiment. This equipment is made for the assembled unit and is portable by a vehicle with volume of 1 m³.

Figure 2.2 (a) and (b) show the diagram of the equivalent circuit and the photograph of the high-voltage pulsed power system, respectively. As stated above, the high-voltage pulsed power system consists of the high-voltage DC power supply with 1 kW power (maximum voltage: 72kV, maximum current: 12mA) and the high-voltage capacitor with the capacitance 1.00, 5.22, and 10.37 μ F. In charging the electrical energy, the charging resistor R_C with 10 k Ω is installed between the high-voltage DC power supply and high-voltage capacitor with consideration for RC time. To remove the electrical energy remained in capacitor after breakdown, the dump resistor R_d with 400 k Ω also is installed in parallel to the capacitor. Furthermore, all of the switches are designed based on the mechanical switch operating pneumatically and the pneumatic system is controlled by solenoid valve. This valves is controlled remotely by 5V TTL signal for the safety.

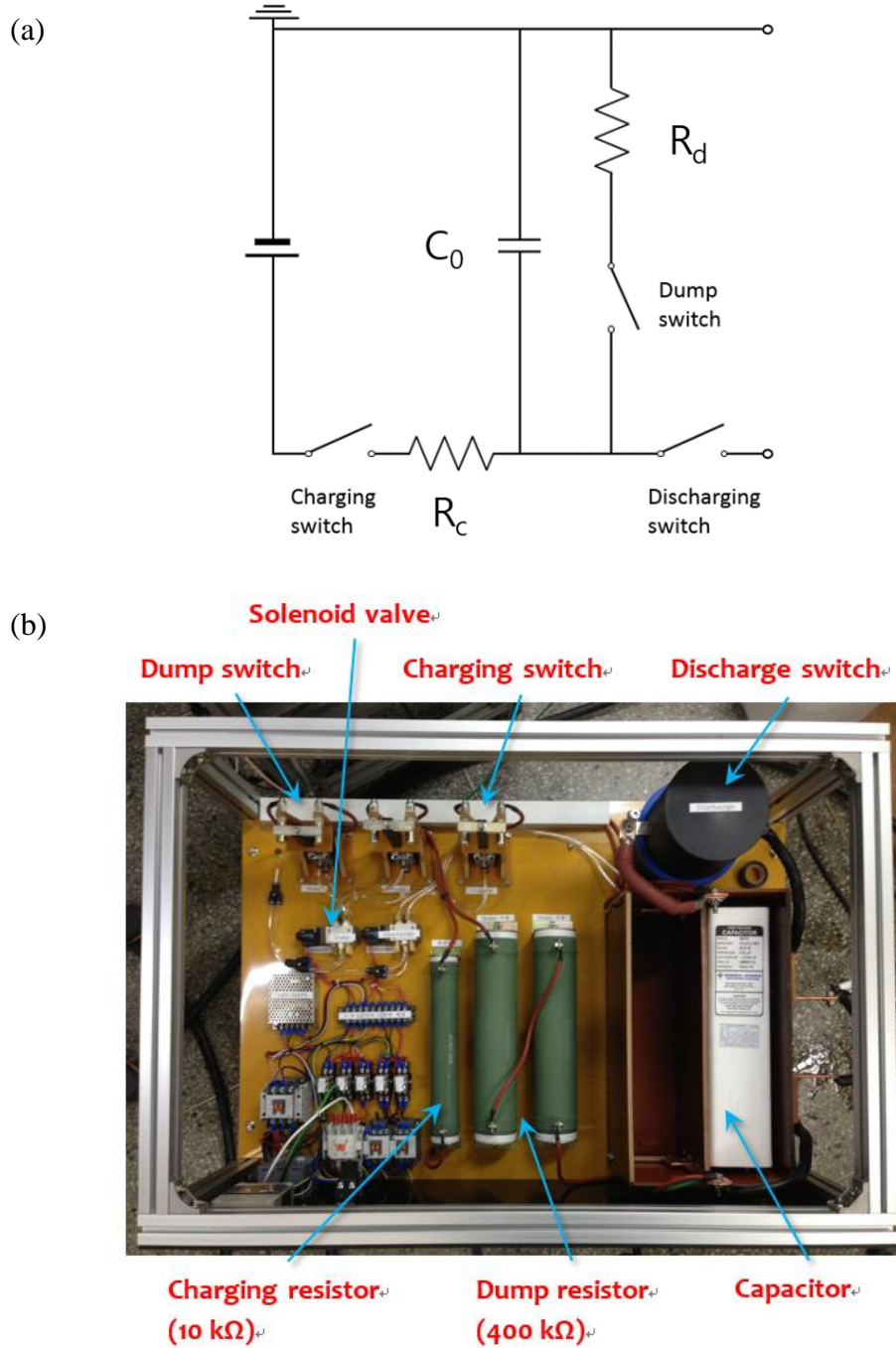


Figure 2.2 (a) Equivalent circuit diagram of high-voltage pulsed power system, (b) photograph of the high-voltage pulsed power system.

2.1.2 Discharge Electrode

The design of the electrode is significant for the repeatability of the electrical discharge experiments, because the electrode have a risk of the destruction by the impact of the spark channel. Figure 2.3 (a) shows the damaged cathode after thousands of times breakdown in practice. To solve the problem of the electrode's short life time, the two improvements is adopted for the design of the electrode. First, the tungsten, which have a high resistance to sputtering or erosion, is used as a material of the electrode and the dome type is adopted as an electrode shape, as shown in Figure 2.3 (b). Second, when the electrode and the electrode supporter as made by insulator are assembled, the rubber O-ring is inserted between the electrode and insulator as shown in Figure 2.4. The rubber O-ring prevent the water penetration into the inner side of insulator cover and relieve the impact of the spark channel on the electrode. After the improvement of the electrode design, the improved electrode withstand the impact of the spark channel with tens of thousands of times breakdown.

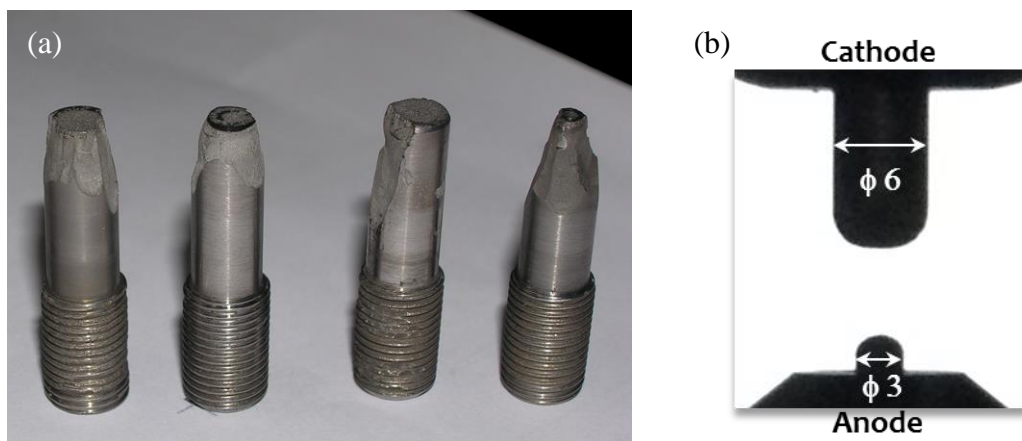


Figure 2.3 a) The damaged cylindrical shape electrode after the breakdown, (b) the improved electrode with dome type structure.

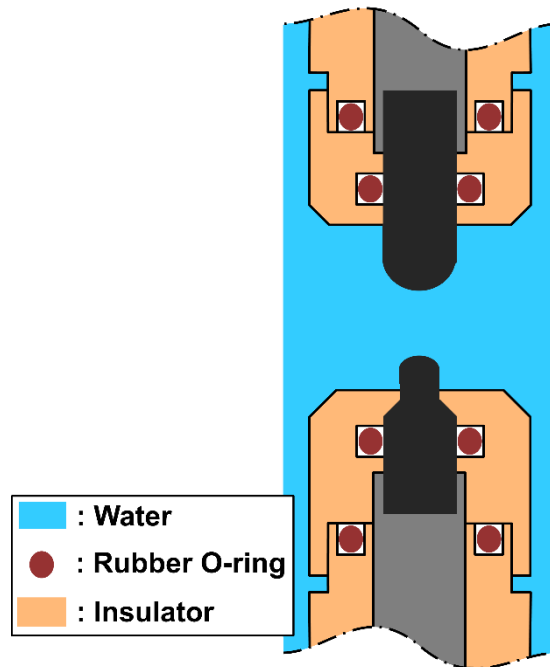


Figure 2.4 Schematic diagram of the improved electrodes at side cross-sectional view with rubber O-ring.

In addition to the improvement of the electrode design, the electrode installation is modified for the repeatability of the electrical discharge experiments. In previous experiment, the bubble formed in the interface between the electrode and insulator cover is critical problem for producing a consistent spark channel. When this bubble exist in the interface between the electrode and insulator cover, the breakdown starts at this area. Then, the insulator cover is damaged or broken, and the spark channel is shown as bend shape. To eliminate the bubble, the anode, in which the breakdown occurs, is installed at bottom side of the discharge chamber. In addition, the clean surface of the anode is obtained by first breakdown.

Finally, the heated electrode interrupts the repeatability of the electrical discharge experiments. If the next experiment is carried out immediately after

previous experiment, the two experimental results of the voltage and current differ considerably. Therefore, the electrode cooling time i.e. 10~20 min. is necessary for reducing this error.

2.2 Diagnostics of Electrical Characteristics and Pressure

The applied voltage at the water gap is computed from the difference between the two applied voltage at the anode and the cathode. As shown in Figure 2.1, the two high-voltage probes are located at the end of the electrode. For this reason, the phase difference between the measured voltage and current is shown and the value of the voltage difference does not actually correspond to the voltage applied at the water gap. To compensate this error, it is needed to measure the circuit parameters of the electrode such as the resistance and the inductance through the short-circuit test.

The short-circuit test is carried out with the capacitance 5.22 μF , the charging voltage 4 kV. In short-circuit test, the relationship of the measured voltage difference (V_{short}) applied across the both sides of the electrode and the current (i_{short}) flowing through the circuit can be written as

$$V_{short} = L \frac{di_{short}}{dt} . \quad (2.1)$$

Figure 2.5 (a) shows the measured voltage difference and current waveform in short-circuit test. The ratio of the measured voltage difference and current is the inductance (L) of the electrode. The inductance L of the electrode leads is an approximately 0.28 μH which is computed from Eq. (2.1). The value of the resistance across the both side of the electrodes is very low with approximately 1 $\text{m}\Omega$, and the voltage drop term by the resistance (iR) is neglected in Eq. (2.1).

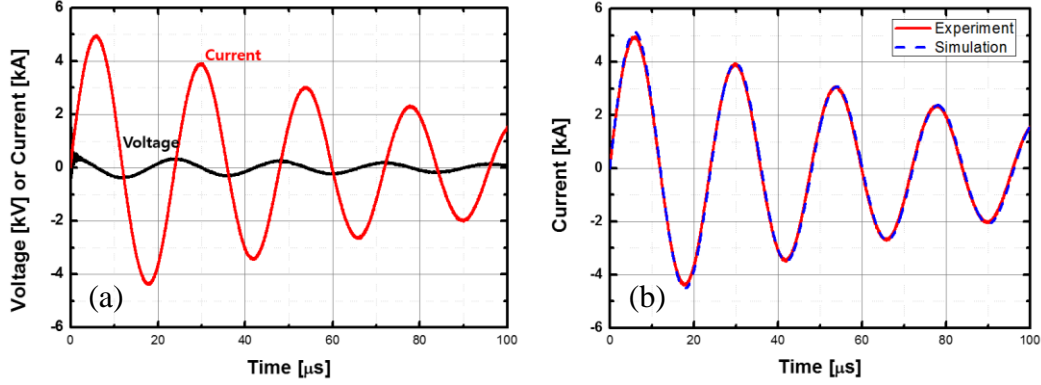


Figure 2.5 Experimental results of short-circuit test: (a) measured voltage difference and current in short-circuit test with the capacitance of 5.22 μF and the charging voltage of 4 kV, (b) comparison of the current waveform in experiment and simulation.

The current flowing through the short circuit is determined theoretically in RLC circuit from the differential equation as follows

$$\frac{d^2i}{dt^2} + \frac{R}{L} \frac{di}{dt} + \frac{1}{LC} i = 0. \quad (2.2)$$

By solving Eq. (2.2) using the initial conditions

$$i(0) = 0, \quad \left. \frac{di}{dt} \right|_{t=0} = \frac{V_0}{L}, \quad (2.3)$$

the current $i(t)$ is obtained as follows

$$i(t) = -\frac{V_0}{\omega_d L} e^{-\beta t} \sin(\omega_d t), \quad (2.4)$$

where

$$\omega_d = \sqrt{\frac{1}{LC} - \left(\frac{R}{LC}\right)^2} \quad (2.5)$$

$$\beta = \frac{R}{2L}$$

Table 2.1 Electrical parameters of the pulsed system in the short circuit test.

Parameter [Unit]	Notation	Value
Capacitance [μF]	C	5.22
Resistance [$\text{m}\Omega$]	R	60
Inductance [μH]	L	2.8
Charging voltage [kV]	V_0	4

V_0 is the charging voltage i.e. 4 kV, R is the resistance of the circuit i.e. 60 m Ω , L is the inductance of the circuit i.e. 2.8 μH and C is the capacitance of the circuit i.e. 5.22 μF . In Figure 2.5 (b), it is assured that the current of simulation is correspond with the current of the experiment.

The resistive voltage (V_r) applied across the spark channel is obtained from the Eq. (2.6).

$$V_r(t) = V_g(t) - L \frac{di(t)}{dt}, \quad (2.6)$$

where V_r is the resistive voltage applied across the spark channel, V_g is the measured gap voltage applied across the electrode, L is the inductance of the electrode leads i.e. 0.28 μH obtained from the short-circuit test and $i(t)$ is the measured current of the experiment.

Figure 2.6 shows the typical waveform of the voltage, current and pressure. As shown in Figure 2.6, the phase difference exists between the measured gap voltage and the current. However, the phase difference is compensated between the resistive voltage and the current by eliminating the inductive voltage term from the measured gap voltage applied across the electrode. The power delivered to the spark channel is calculated by multiplication of the resistive voltage and the current.

The spark channel is regarded as cylindrical geometry, because the initial

radius of the spark channel is much narrower than the gap distance. And the channel radius is still below the gap distance at the time of the shock wave formation, as discussed in Sec. 4.2. Consequentially, the spark channel is regarded as cylindrical geometry. However, the formed shock wave propagates into water as a spherical sound waveform of which the amplitude diminishes inversely as the distance from the axis of the spark channel. As shown in Figure 2.7, the pressure amplitude, which is measured at intervals of 10 mm, correspond to $\sim r^{-1}$ [23]. The propagated pressure wave is detected by the piezoelectric sensor located at 100 mm away from the axis of the spark channel. And the pressure wave propagates in water with the sound velocity as shown in Figure 2.8.

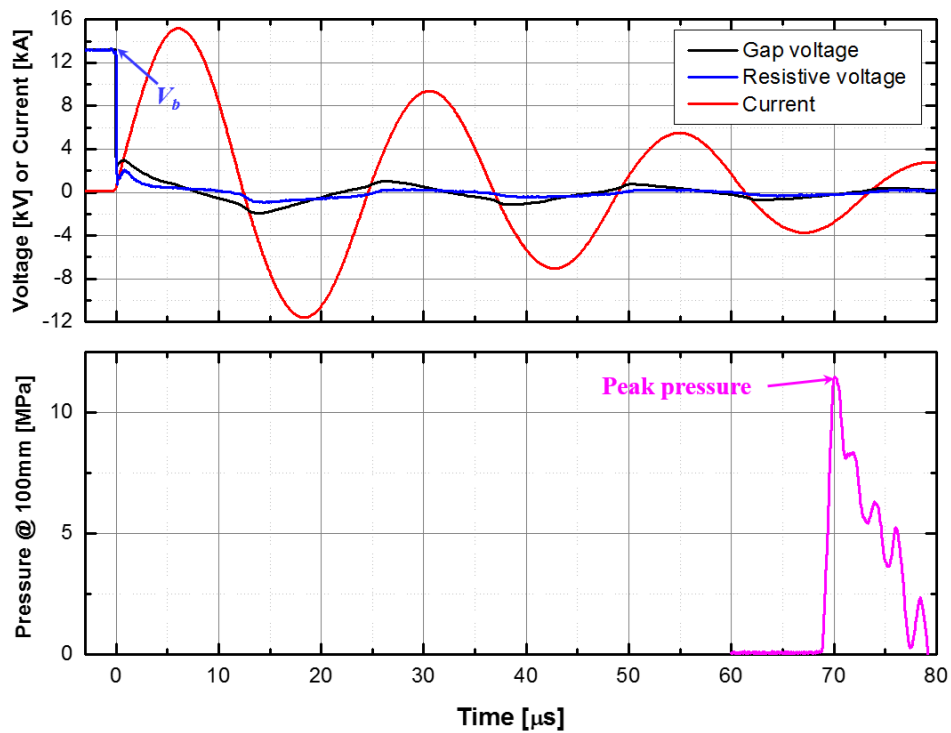


Figure 2.6 Typical waveforms of the gap voltage (V_g), resistive voltage (V_r), current and pressure. The resistive voltage is obtained by subtraction inductive voltage term from the measured gap voltage across the electrode.

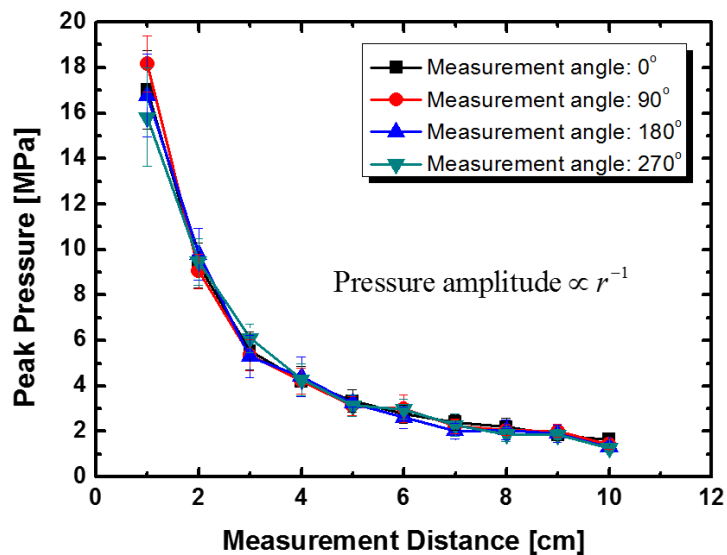


Figure 2.7 The pressure amplitudes is measured at intervals of 10 mm. The pressure amplitude decreases inversely as the distance from the axis of the spark channel, irrespective of measurement angle. Determination of the measurement angle based on the axis of the spark channel at top view.

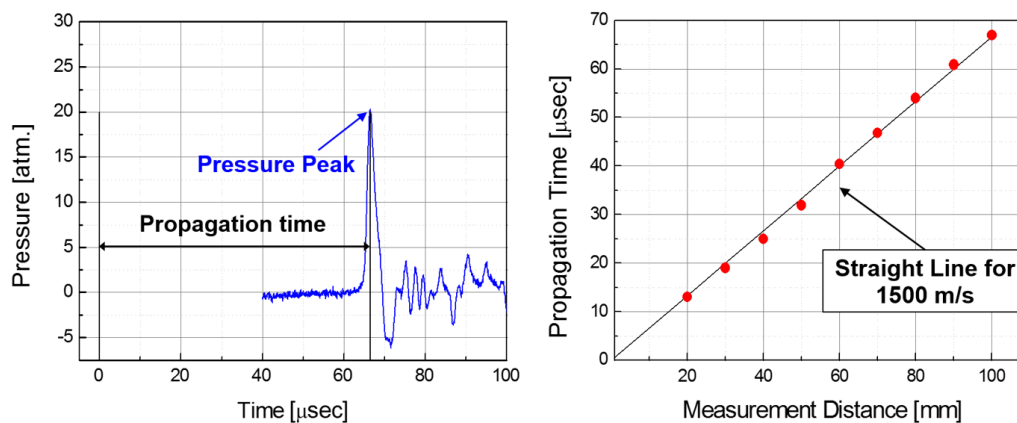


Figure 2.8 Propagation of the pressure wave with the sound velocity.

Chapter 3 Pre-breakdown Process

3.1 Bubble formation and Streamer Discharge in Bubble

In UPSD, the time delay always is observed before the breakdown. As shown in Figure 3.1, the voltage applied across the electrode ($t = 0$) decreases gradually before the voltage drops rapidly ($t = 1.62$ ms). The gradually declining period of the voltage is the time delay and this time delay is varied by the experimental condition such as gap distance, capacitance and charging voltage. This period of the time delay is stated as the pre-breakdown. To verify what happened for the pre-

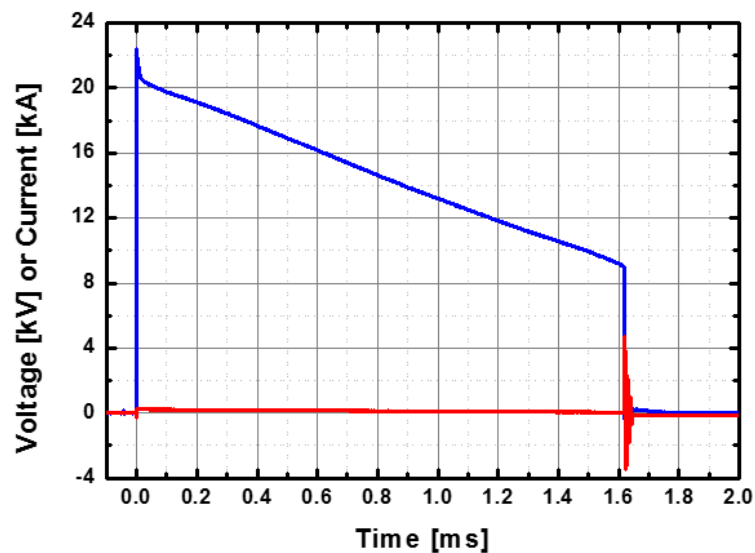


Figure 3.1 Typical waveform of the voltage and the current in UPSD with capacitance of $1 \mu\text{F}$, gap distance of 6 mm and charging voltage of 20 kV.

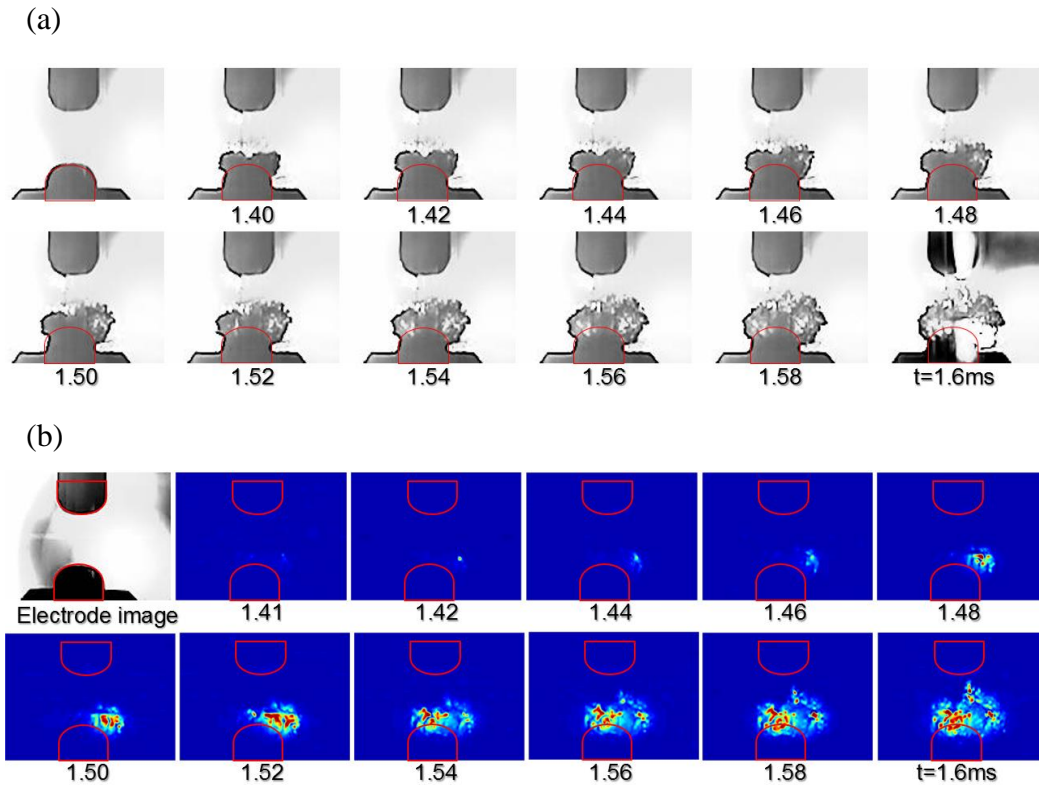


Figure 3.2 (a) corresponding raw images of the bubble generation with a back light, and (b) converted color images of the streamer evolution without back light during the pre-breakdown phase taken by fast CCD camera.

breakdown, the process of the pre-breakdown is observed and recoded by a fast CCD camera.

Figure 3.2 shows the raw images of the pre-breakdown process with back light, and the converted images of the pre-breakdown process without back light with capacitance of $1 \mu\text{F}$, gap distance of 6 mm and charging voltage of 20 kV. As stated in Chapter 2, the photographs of the pre-breakdown in the water gap are taken in every $10 \mu\text{s}$ with $1 \mu\text{s}$ of exposure time by fast CCD camera and the frame

size of the photograph is 144x108 pixels. In the first photograph of Figure 3.2 (b), the photograph is taken with a back light. For this reason, subjects such as the electrode, which interrupt the light propagation, are shown as black shadow images. Therefore, the first image of the upper left side is the electrode and the rest of the images show the bubble generation at anode before the breakdown in Figure 3.2 (b). The photograph of Figure 3.2 (c) is taken without back light to assure the existence of the light emission in gas bubble before the breakdown. Those photographs are converted into colored images by image processing with a software (Matlab). As a result, it is assured that the streamer discharge occurs in bubble before the breakdown.

To define the process of the pre-breakdown precisely, the scale of current is magnified by 1000 times. Figure 3.3 shows the measured current during the pre-breakdown phase with capacitance of 1 μF , gap distance of 7 mm and charging voltage of 17 kV. The current with a few A leaks through the water gap during the

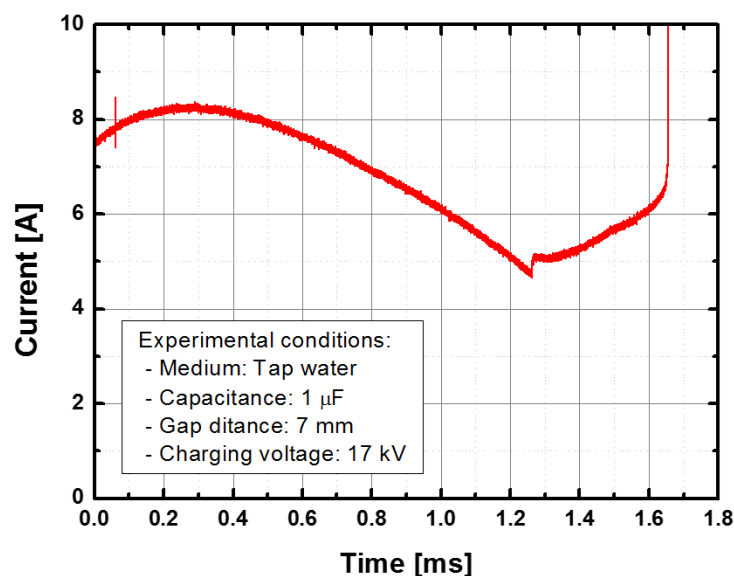


Figure 3.3 The current flowing in the water gap for the pre-breakdown with capacitance of 1 μF , gap distance of 7 mm and charging voltage of 17 kV.

pre-breakdown phase and current peak appears at 0.3 ms. This leakage current heats the water at the surface of the anode and this heating by a leakage current leads to the bubble generation. Moreover, the current jump is abruptly observed at 1.26 ms and the streamer discharge occurs in the bubble at this time. In the plot of current, the time at which the streamer discharge occurs can be identified, while the time at which the bubble is formed cannot be identified. Therefore, the resistance plot of the water gap during the pre-breakdown phase is understood with corresponding images of the pre-breakdown process as shown in Figure 3.4. The initial resistance of the water gap is approximately 2300 Ω and the resistance of the water gap decreases gradually until 0.9 ms and the resistance of the water gap reaches the minimum value at 0.9 ms before the streamer discharge occurs. After the time of 0.9 ms, the resistance of the water gap increases since the gas bubble, which has low conductivity compared with liquid water, is formed at the anode. As the voltage applied across the gas bubble reaches the breakdown voltage, the streamer is generated in the gas bubble. The streamer generation can be confirmed by the light emission at 1.26 ms in Figure 3.4, and the steepening in the resistance of the water gap occurs at this time as well. After this time, the streamer and gas bubble is propagating to the cathode until breakdown. Therefore, the pre-breakdown phase proceeds in four stage: (i) water heating, (ii) gas bubble generation and expansion, (iii) electron avalanche, and (iv) streamer propagation to the cathode.

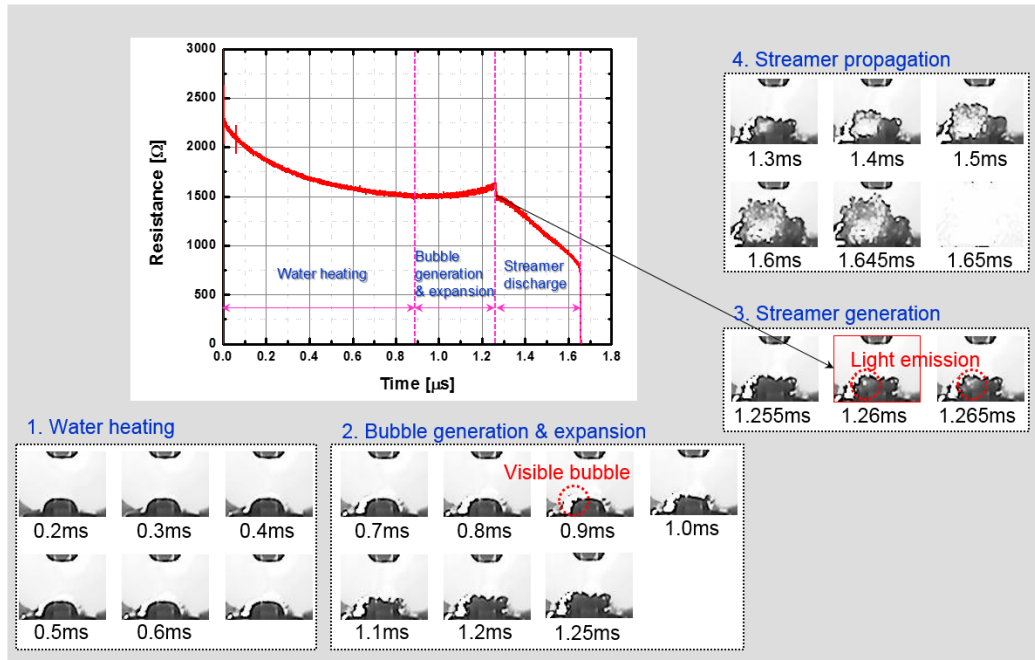


Figure 3.4 The resistance of the water gap for pre-breakdown phase and corresponding images of the pre-breakdown process with capacitance of 1 μF , gap distance of 7 mm and charging voltage of 17 kV.

3.2 Energy Consumption during Pre-breakdown

The initial energy stored in the capacitor delivers to the water gap during the pre-breakdown phase. This energy is used for bubble generation and streamer discharge as shown in the previous section. To know how to consume the energy during the pre-breakdown phase, the energy consumption is estimated by changing the experimental conditions such as gap distance and charging voltage. The energy is calculated by the multiplication of the measured DC voltage and current and the energy for each stage of the pre-breakdown is classified by using the resistance

plot.

As a result, the energy consumed for each stage of the pre-breakdown phase with various gap distances and charging voltages is shown in Figure 3.5. The considerable portion of the total spent energy for the pre-breakdown phase is used to heat water and form the gas bubble in all experimental conditions. Moreover, the variation of the energy for water heating is low in comparison with the energy consumed for other stages, because the energy for water heating is influenced only by the geometry of the electrode. As the gap distance is larger, the energy for water heating increases. For instance, the average energy for heating water in the gap distance of 5 mm is approximately 70 J, while the average energy for heating water in the gap distance of 10 mm is approximately 90 J.

The energy consumed for other stages of the pre-breakdown except for the stage of water heating shows big difference with increasing the gap distance. In short distance, the energy consumed for bubble expansion and streamer propagation is extremely low in all charging voltages. In the long distance, on the other hand, the energy consumed for bubble expansion and streamer propagation is relatively high in comparison with that of the short distance.

As increasing the charging voltage, the energy consumed for bubble expansion and streamer propagation increases until the specific charging voltage. And after the specific charging voltage, the energy consumed for bubble expansion and streamer propagation decreases. In low charging voltage, the generated bubble expands extensively, therefore the density of the bubble is low. In high charging voltage, however, the streamer discharge occurs as soon as the bubble is generated, eliminating energy consumption for the streamer as shown in Figure 3.5.

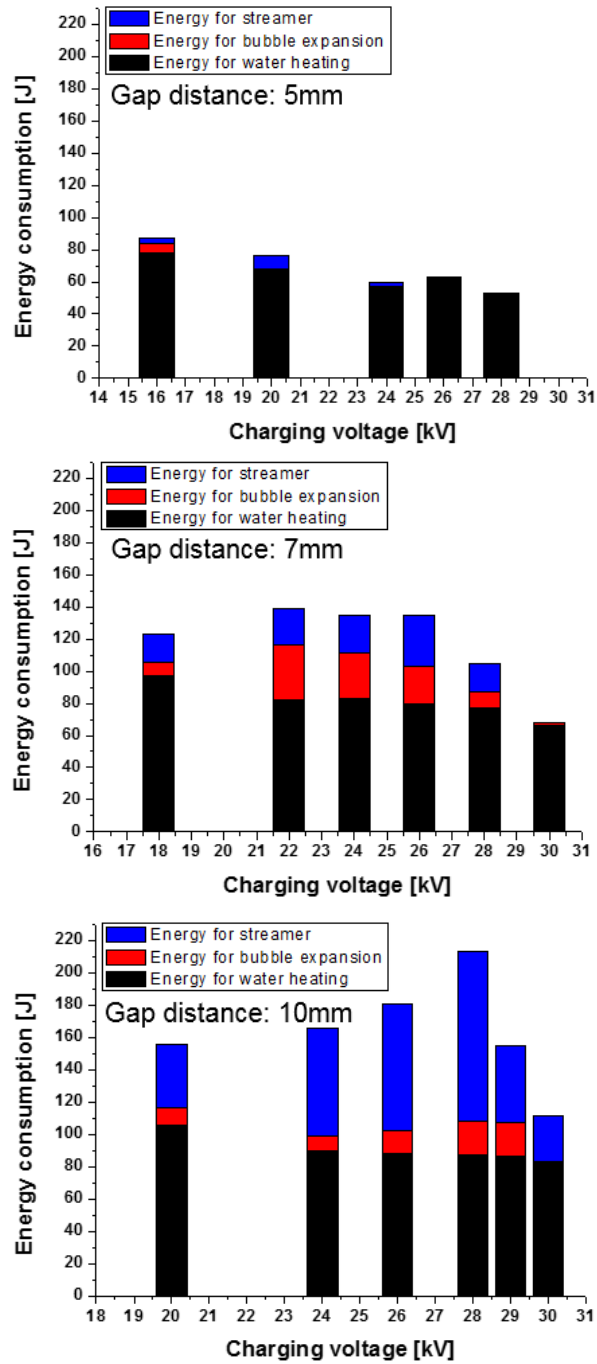


Figure 3.5 Energy consumed for the each stage of the pre-breakdown phase with various charging voltage and gap distance.

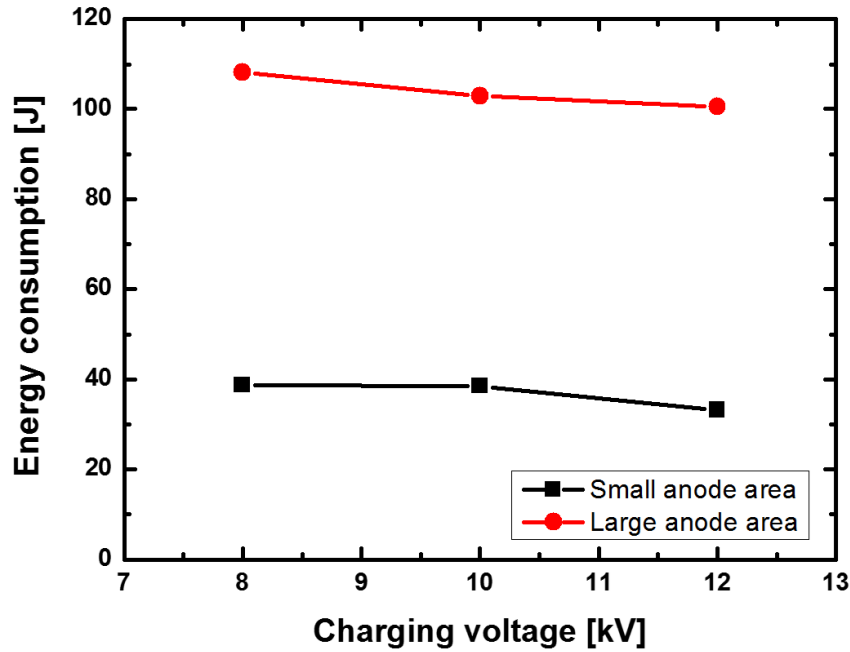


Figure 3.6 Comparison of the energy consumption for the pre-breakdown phase versus charging voltage and anode area with capacitance of 1 μF and gap distance of 5 mm. (anode area ■: $9\pi \text{ mm}^2$, ●: $18\pi \text{ mm}^2$)

Figure 3.6 shows the effect of anode area on the energy consumed for pre-breakdown phase. As mentioned above, the considerable portion of the total energy for the pre-breakdown phase is used to heat water and form the gas bubble. Because the gas bubble is generated at anode surface, the energy for water heating and bubble generation decreases as decreasing the anode area. The energy for water heating and bubble generation of small anode area is lower than that of the large anode area. Therefore, the energy consumed for pre-breakdown phase can be reduced by reducing the anode area.

3.3 Initial resistance of the spark channel

As shown in Figure 3.7, the bubble expands with large volume in case of low charging voltage, whereas the bubble, in case of high charging voltage, does not practically expand in comparison with the volume of the bubble in low charging voltage. In case of low charging voltage, it is expected that the density in the bubble becomes lower and the streamer is generated with occupying the wide area of the bubble cross section. In case of high charging voltage, on the other hand, the streamer discharge occurs as soon as the bubble is generated with narrow area. Consequently, as increasing the charging voltage, it is expected that the cross section of the spark channel becomes narrow and the plasma density increases. Therefore, the initial resistance of the spark channel increases as increasing the charging voltage.

As shown in Figure 3.8, the initial resistance of water gap is similar at 2300 Ω in all charging voltages in the identical experimental condition. However, as increasing charging voltage, the resistance of the water gap decreases faster while the initial resistance of the spark channel at low voltages reaches much smaller value by forming streamers. For example, the initial resistances of the spark channel are approximately 1200 Ω at the charging voltage of 26 kV before breakdown, but from 1500 Ω to 750 Ω with streamer formation at the charging voltage of 17 kV, respectively. It is expected that the higher initial resistance of the spark channel leads to increase the power delivered to the spark channel at early stage of discharge. It will be discussed in Chap. 5.

Charging voltage	Bubble size at time of streamer formation	Breakdown voltage
17kV		7.6 kV
18kV		9.2 kV
20kV		12.8 kV
22kV		15.0 kV
24kV		18.6 kV
26kV		21.1 kV

Figure 3.7 Comparison of the bubble size as varying charging voltage with capacitance of 1 μ F and gap distance of 7 mm.

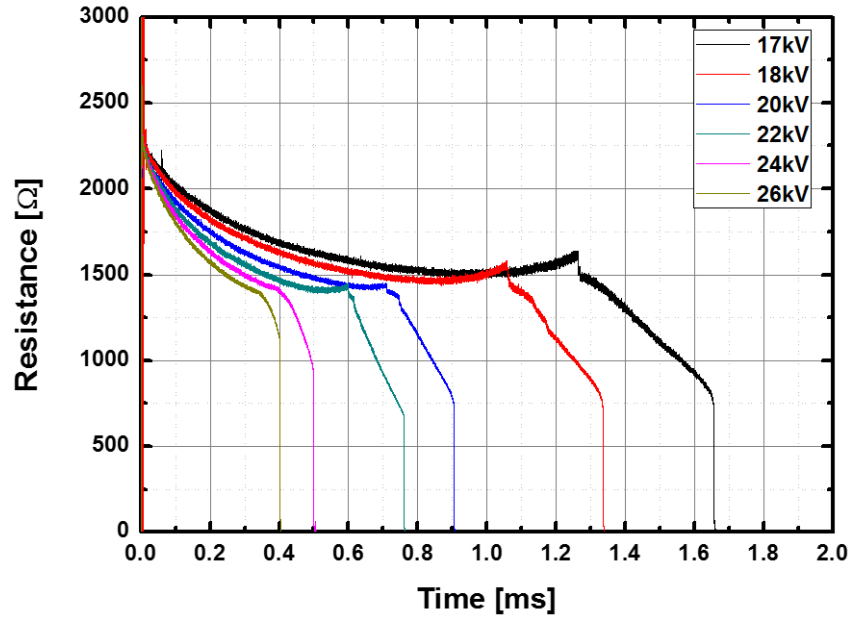


Figure 3.8 Plot of the resistance of water gap versus the charging voltage during the pre-breakdown phase with capacitance of 1 μF and gap distance of 7 mm.

Chapter 4 Mechanism of the Shock Wave Formation

4.1 Shock Wave Formation by an Expanding Spark Channel

To investigate how to form the shock wave in UPSD, it is necessary to understand the principle of shock wave formation by an accelerating piston in fluid [24, 25, 26]. Figure 4.1 shows a brief description of the process of the shock wave formation by an accelerating piston. If the piston initially moves into the gas at a low speed and is gradually accelerated, the shock wave is not formed immediately. As shown in Figure 4.1, the first compression wave is generated and propagates with the speed of sound when the piston move to the stationary fluid. As the speed of the piston increase more, the second compression wave propagates with higher speed, which is the sum of the speed of sound and piston speed, than that of the first compression wave. Therefore, the later formed compression wave overtakes the preceding compression wave, because the later formed compression waves is faster than preceding waves. As a result, a steepening in the density and the pressure occurs at the specific time and position of accumulation of the compression waves, and then the shock wave is formed.

The process of the shock wave formation in UPSD is analogous to the process of the shock wave formation by an accelerating piston. The generation of the compression waves by an expanding spark channel is depicted in Figure 4.2.

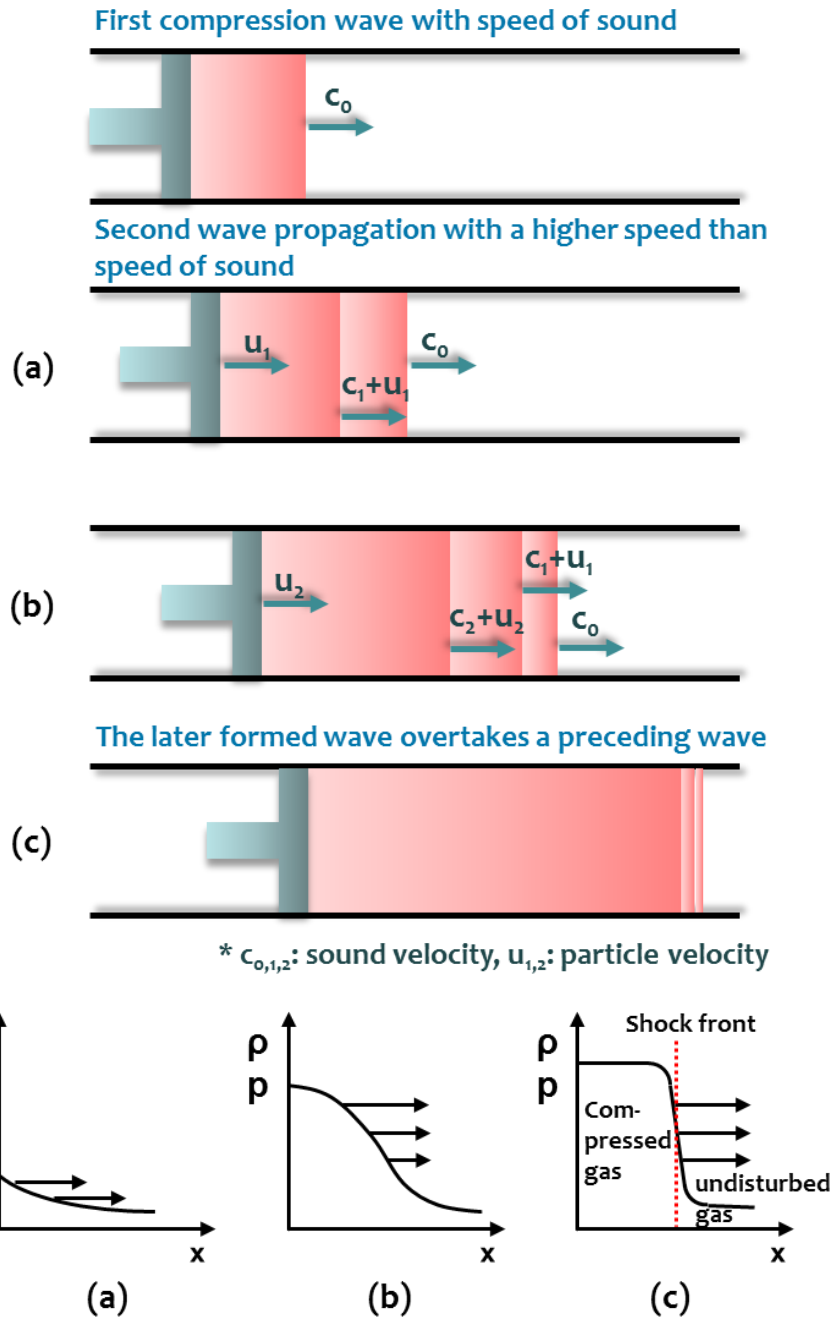


Figure 4.1 Schematic diagram of the mechanism of the shock wave formation by an accelerating piston in fluids.

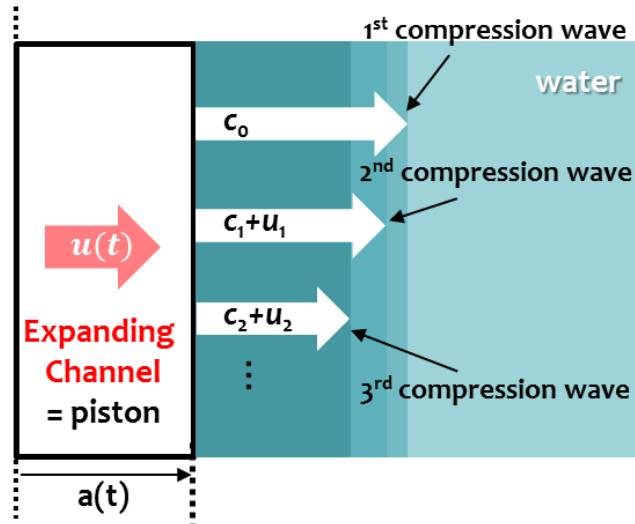


Figure 4.2 Schematic diagram of the generation of the compression waves by an expanding spark channel.

In UPSD, the expanding spark channel acts like a piston. As the expansion of the spark channel proceeds, the additional compression waves arise with the speed of the channel speed added to the speed of sound.

The generation of a shock wave by an underwater spark discharge is more complicated than that of the accelerating piston in that the radial acceleration of the spark channel is accomplished by time-varying external Joule heating. It is expected that the spark channel can't accelerate consistently and it is assumed that the acceleration period could exist in expanding the spark channel. This supposed circumstance is depicted in Figure 4.3. For an accelerating spark channel with a time-varying channel expansion speed, the accumulation of waves contributing to shock wave formation will take place until the channel expansion speed reaches the maximum value. Hence, the amplitude of the underwater shock pressure measured at a position sufficiently far from the spark channel is recognized to be proportional to the energy absorbed during the accelerating phase

of the spark channel. Therefore, it is important to find out the time of maximum channel expansion speed (t^*).

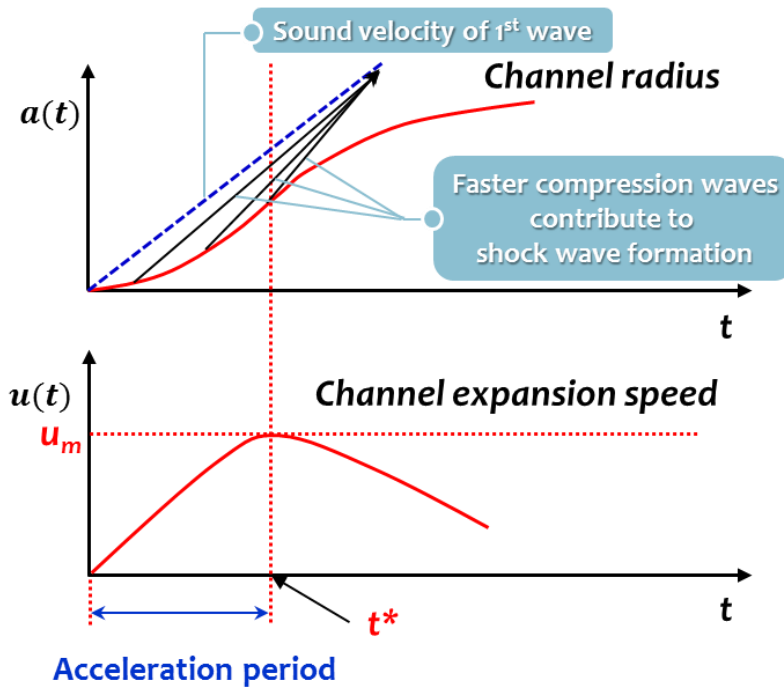


Figure 4.3 Schematic diagram of the generation of the compression waves by an expanding spark channel.

Figure 4.4 (a) is a schematic diagram for calculating the time of accumulation of the compression waves during the acceleration period. As shown in Figure 4.4 (b), the initial compression wave and the last compression wave, which are formed until the channel expansion speed reaches the maximum value, meet at specific time, t_F . Assuming the radius and speed of the initial compression wave are a_0, c_0 and the radius and speed of the in last compression wave are $a_m, c_0 + u_m$ respectively, the time of accumulation of the compression waves, t_F

is described as follows,

$$c_0 t_F = (c_0 + u_m) \times (t_F - t^*) + (a_m - a_0). \quad (4.1)$$

Equation (4.1) is rearranged by the time of accumulation of the compression waves, as described below,

$$t_F = \frac{(c_0 + u_m)}{u_m} t^* - \frac{(a_m - a_0)}{u_m}, \quad (4.2)$$

If it is assumed that $u_m = 350 \text{ m/s}$, $a_0 = 0.2 \text{ mm}$, $a_m = 0.6 \text{ mm}$, $t^* = 1 \mu\text{s}$, t_F is calculated as $4 \mu\text{s}$. Therefore, the shock wave is formed within a few micro second after the onset of breakdown.

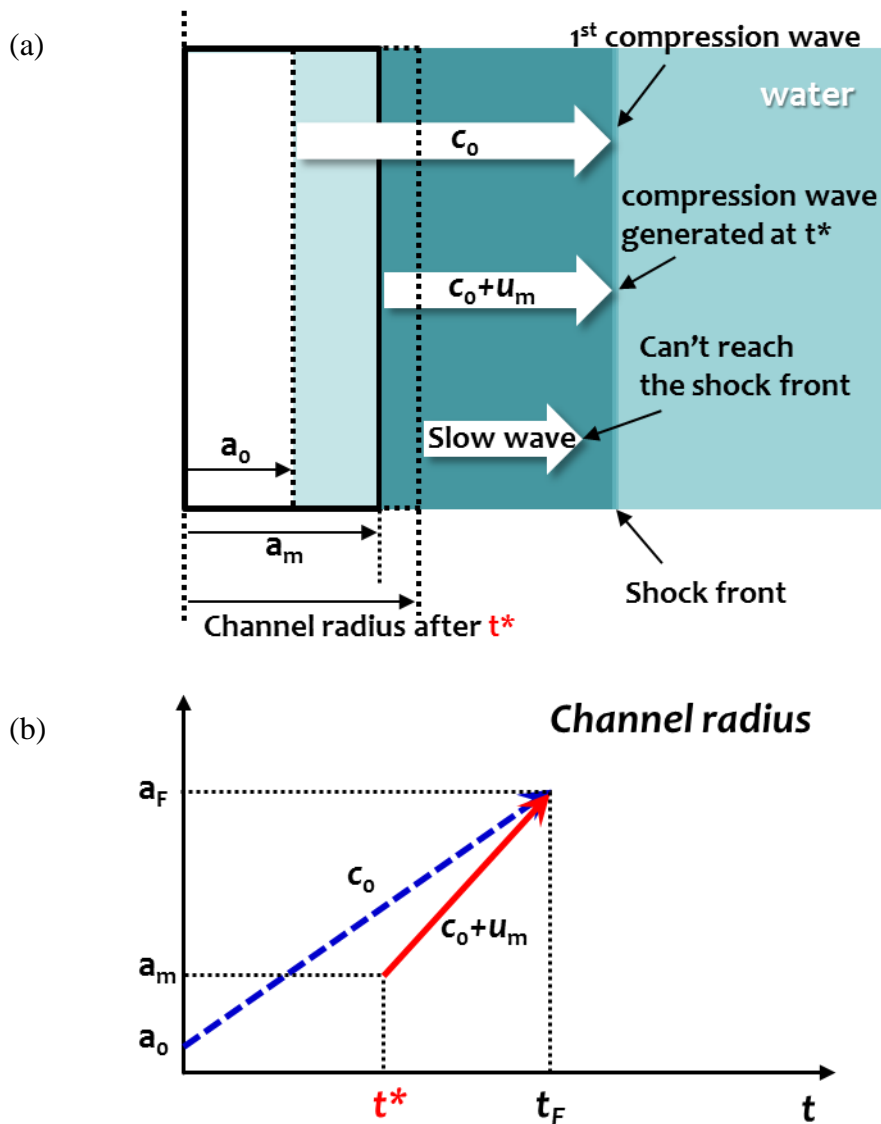


Figure 4.4 (a) Schematic diagram of the accumulation of the compression waves for the time of maximum spark channel expansion speed, (b) the time-distance graph of two compression wave at $t = 0$ and $t = t^*$.

4.2 1D Model for Spark Channel Expansion

Since the time-varying channel expansion speed is very hard to measure directly, the alternative method for obtaining the spark channel expansion speed is required. To suggest an alternative method, it is needed to know the pressure of the spark channel in condition of the shock wave formation. Figure 4.5 shows the schematic diagram of the distribution of the pressure at the time of shock wave formation.

When the shock wave is formed, the pressure inside the shock front is supposed to be uniform, because the width of the shock front is narrow. And the pressure of the spark channel and that of the shock front are identical at the interface of the spark channel and shock front. Therefore, the pressure in the spark

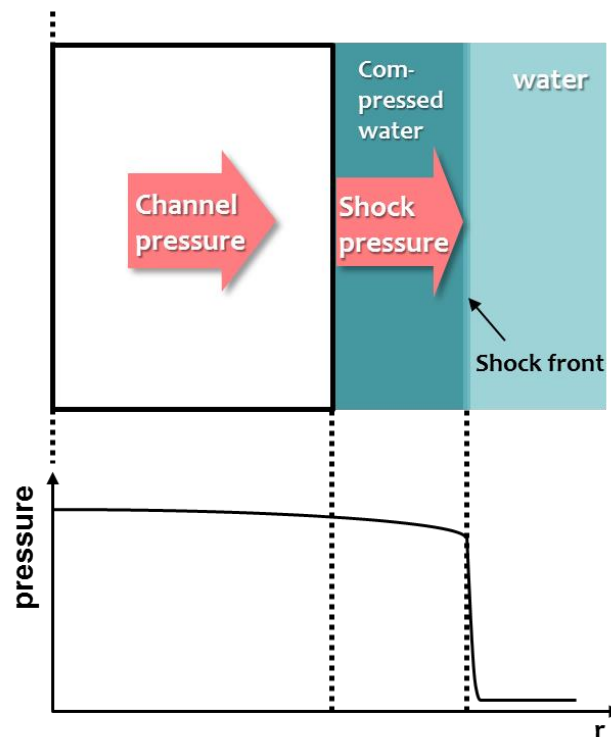


Figure 4.5 Schematic diagram of the distribution of the pressure under the shock wave formation.

channel can be assumed to be the pressure of the shock front, and the shock approximation can be determined as following [27].

The mass and motion of water particle are conserved across the shock front ($r = a_c$) in Figure 4.6. The two conservation equations can be written as

$$\frac{\partial \rho}{\partial t} + \nabla \cdot (\rho v) = 0, \quad (4.3)$$

$$\rho \frac{\partial v}{\partial t} + \rho (v \cdot \nabla) v = -\nabla p, \quad (4.4)$$

If the density, velocity and pressure in undisturbed water are assumed to be (ρ_0, v_0, p_0) and those in compressed water are assumed to be (ρ, v, p) , the above two Eqs. (4.3) and (4.4) can be written as

$$\rho v = \rho_0 v_0 = \rho_0 \frac{da_c}{dt}, \quad (4.5)$$

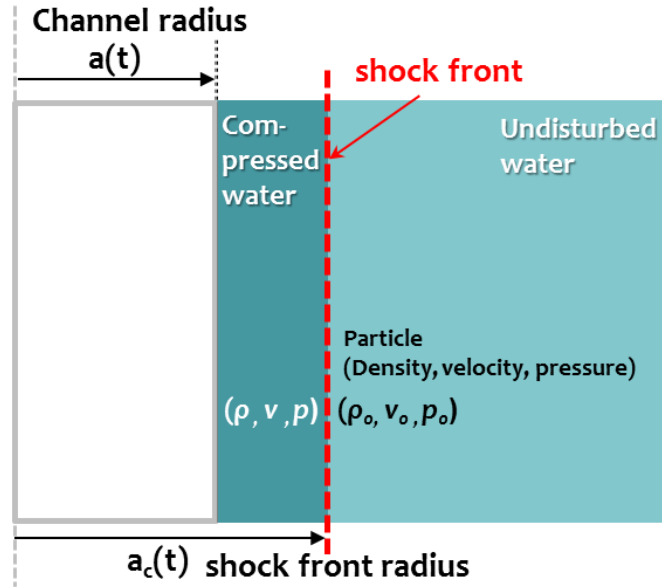


Figure 4.6 Schematic diagram of density, velocity and pressure of two regime across the shock front.

$$p_0 + \rho_0 v_0^2 = p + \rho v^2, \quad (4.6)$$

where the particle velocity ahead of the shock is replaced by the shock velocity ($v_0 = da_c/dt$). To compute the shock approximation, the well known equation of state of water is needed.

$$p = c_1 (\rho/\rho_0)^{\gamma_1} - c_2, \quad (4.7)$$

where $\gamma_1=7$, $c_1 = 3.001 \times 10^8$ MPa, $c_2 = 3.000 \times 10^8$ MPa. If the Eqs. (4.5), (4.6) and (4.7) are solved, assuming $p \gg p_0$, the shock approximation is obtained as follows,

$$p = \rho_0 \left(\frac{da_c}{dt} \right)^2 \left[1 - \frac{1}{(p/c_1 + c_2/c_1)^{1/\gamma_1}} \right]. \quad (4.8)$$

Braginskii modified this equation as follows [28],

$$p = K_p \rho_0 \left(\frac{da}{dt} \right)^2, \quad (4.9)$$

where ρ_0 is the mass density of water at room temperature, i.e. 10^3 kg m^{-3} . The proportionality coefficient K_p is assumed to be 2 [27, 29].

As stated above, the direct measurement of the time-varying channel expansion speed, especially the maximum value of the channel expansion speed, is very difficult because the variation of the channel expansion speed occurs in a very short time. Therefore, it is necessary to find out the alternative method for obtaining the spark channel expansion speed. This section presents that the channel expansion speed is indirectly estimated by using a simple power balance equation. In developing the simple power balance equation, it is assumed that the spark channel is a straight cylinder and that it expands only in the radial direction with a time-varying channel radius $r(t)$ or channel cross-sectional area $A(t)$. The electrical

energy delivered to the spark channel by Joule heating is the sum of the increase in the internal energy of the spark channel and the work done on the surrounding water. Therefore, the power balance equation can be written as [22, 30]

$$\frac{d}{dt} \left(\frac{p}{\gamma-1} A \right) + p \frac{dA}{dt} = \frac{P(t)}{l}, \quad (4.10)$$

where p is the pressure in the spark channel, l is the channel length, and $P(t)$ is the power delivered to the spark channel. The specific heat ratio γ of the internal energy term is assumed to be 1.3. All of the losses are neglected because the time scale we are interested in is shorter than the characteristic times for radiation or conduction losses [22].

As described in previous section, Braginskii's shock approximation is substitute for the pressure in the spark channel of Eq. (4.10). Therefore, the modified power balance equation can be written as

$$\frac{K_p \rho_0}{2\pi(\gamma-1)} \frac{dA}{dt} \frac{d^2 A}{dt^2} + \frac{K_p \rho_0}{4\pi A} \left(\frac{dA}{dt} \right)^3 = \frac{P(t)}{l}. \quad (4.11)$$

The spark channel expansion speed is obtained by solving Eq. (4.11) using the experimental power data. The initial channel radius is assumed to be 0.2 mm in solving Eq. (4.11) [6].

Figure 4.7 (a) shows the first half-cycle waveforms of measured voltage difference, resistive voltage across the water gap and current flowing through the spark channel. From the resistive voltage and the current waveforms, the Joule heating power delivered to the spark channel $P(t)$ can be simply calculated as depicted in Figure 4.7 (b). The temporal waveform of $P(t)$ has a peak value of 8.7 MW at 2.3 μ s after the onset of the spark discharge, which is quite different from the voltage and the current waveforms where the voltage and the current peaks appear at 0.8 μ s and 6.2 μ s, respectively. The expansion speed of the spark channel calculated from Eq. (4.11) is plotted in Figure 4.7 (c). The spark channel expansion

speed is shown to increase rapidly and reach a maximum value at $1.5 \mu\text{s}$ after the breakdown, denoted as t^* in Figure 4.7 (c). And the energy absorbed by the spark channel (E^*) until $t = t^*$ as

$$E^* = \int_0^{t^*} P(t)dt . \quad (4.12)$$

In Figure 4.7 (d), E^* is calculated to be $\sim 6 \text{ J}$, which is only 1.3% of the energy stored in the capacitor at breakdown. The calculated energy (E^*) determine the peak pressure.

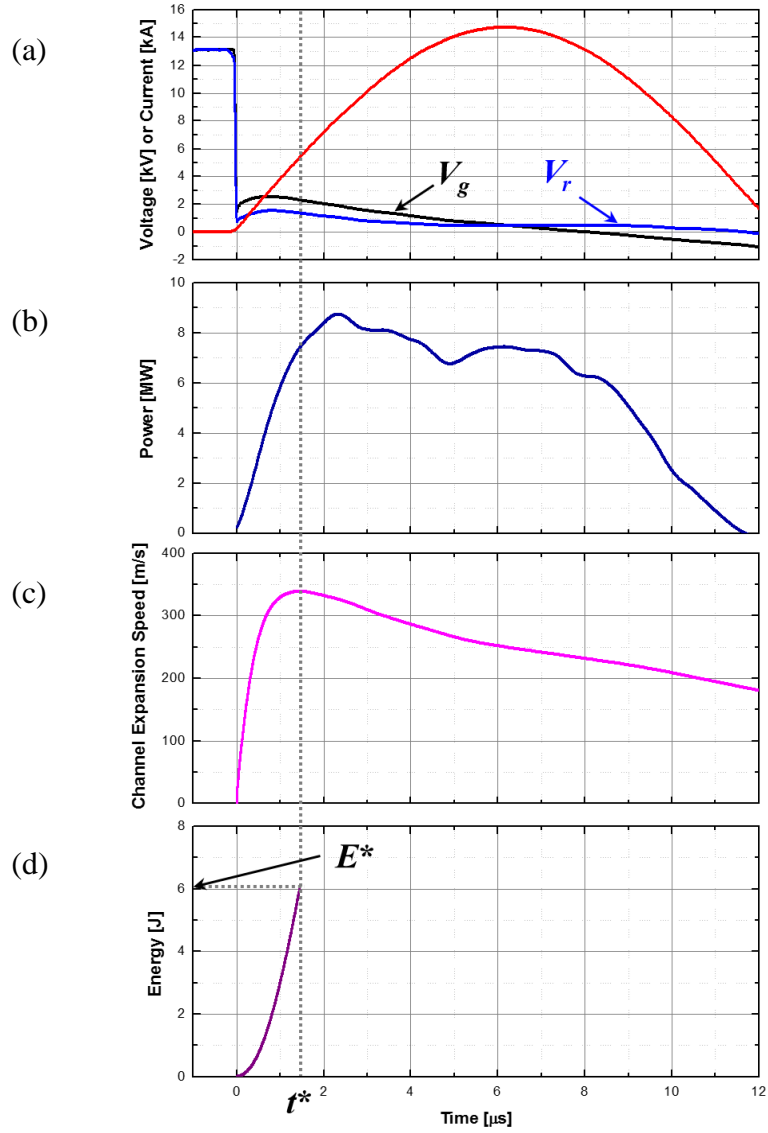


Figure 4.7 (a) The gap voltage (V_g), resistive voltage (V_r) and current waveforms for the charging voltage of 14 kV with a capacitance of $5.22 \mu\text{F}$, (b) the Joule heating power ($P(t) = V_r(t) \times i(t)$), (c) the spark channel expansion speed derived from the power balance model, and (d) the absorbed energy in the spark channel until t^* , where t^* is the time required for the channel expansion speed to reach its maximum.

4.3 Relationship between Peak Pressure and E^*

In previous researches, the peak pressure is affected by the energy stored in the capacitor at breakdown. As described in Sec. 1.3, however, it is assured that the estimated peak pressure is not consistent among previous results of the researchers. Fundamentally, those researches presented that the peak pressure is affected by the remaining energy in the capacitor at breakdown which is expressed in the multiplication of the capacitance and the square of the breakdown voltage ($E_b = \frac{1}{2}CV_b^2$). In Touya's work, the peak pressure was approximately proportional to the cube root of the energy stored in the capacitor at breakdown [9]. Whereas, Timoshkin's work presented that the spark discharges of low capacitance and high breakdown voltage generate stronger peak pressure in the same energy stored in the capacitor at breakdown [22]. Therefore, this section presents what is the determining factor to the peak pressure with consideration for a highly transient and nonlinear phenomenon of UPSD.

Figure 4.8 shows the dependency of the peak pressure on the remaining energy stored in the capacitor at breakdown (E_b) with various charging voltage and capacitance such as the previous researches. The peak pressure has a different slope to the remaining energy stored in the capacitor at breakdown depending on the capacitance. Although the remaining energy stored in the capacitor at breakdown is identical, the peak pressure is higher with the experimental conditions of a lower capacitance and a higher breakdown voltage. It means that all of the energy stored in the capacitor at breakdown does not contribute to form the shock wave and the consumed energy for the shock wave formation is difference depending on the experimental conditions such as the capacitance. Therefore, noble determining factor to the peak pressure is presented with consideration for the transient process of shock wave formation occurring immediately after the onset of a spark

discharge.

As mentioned in Chap. 4, the energy absorbed in the spark channel until the expansion speed of the spark channel reaches its maximum value determines the shock wave formation and the peak pressure. Figure 4.9 shows the dependency of the peak pressure on the energy absorbed during the acceleration phase of the spark channel (E^*) calculated by Eq. (4.11) and experimental power data. Contrary to Figure 4.9, the peak pressure is proportional to the energy absorbed during the acceleration phase of the spark channel irrespective of the capacitance although the standard deviation is somewhat large. Therefore, it is clearly shows that the energy absorbed during the acceleration phase of the spark channel is the key factor to determine the peak pressure.

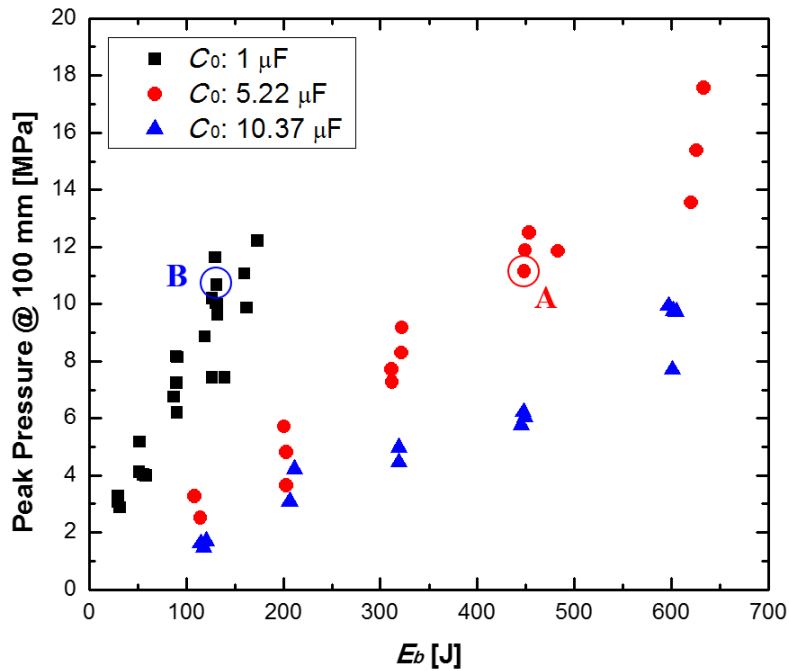


Figure 4.8 Dependency of the peak pressure measured at 100 mm from the axis of the spark channel on the remaining energy stored in the capacitor at breakdown (E_b) with various charging voltage and capacitance.

In Figure 4.9, the two experimental data denoted as “A” and “B” shows the similar peak pressure due to the similar energy absorbed during the acceleration phase of the spark channel. However, those two experimental data shows the different remaining energy stored in the capacitor at breakdown in Figure 4.8. One gas a high remaining energy of 449 J with a high capacitance of 5.22 μF (denoted as “A” in Fig. 4.9), and the other has a low remaining energy of 131 J with a low capacitance of 1 μF (denoted as “B” in Fig. 4.9). Although the remaining energy with a higher capacitance of 5.22 μF is approximately 3.4 times larger than with a lower capacitance of 1 μF , the energy absorbed during the acceleration phase of the spark channel for the two cases is approximately the same as about 6 J, thus

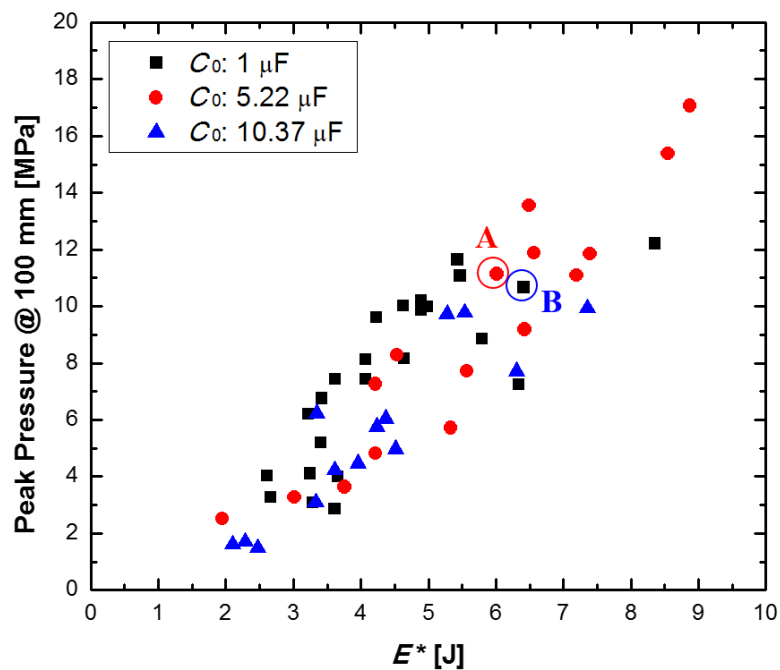


Figure 4.9 Dependency of the peak pressure measured at 100 mm from the axis of the spark channel on the energy absorption in the spark channel until the spark channel expansion speed reaches its maximum value (E^*) with various charging voltage and capacitance.

the measured peak pressure has approximately the same value of about 11 MPa, as depicted in Figure 4.9.

To find out the reason of this difference, the temporal current, power absorption, the channel expansion speed and the energy absorption during the acceleration phase are compared in Figure 4.10. Although the current rising rate of higher capacitance is higher than that of the lower capacitance, the power absorption rate is higher for the case of lower capacitance. This result implies that the resistance of the spark channel decreases with time faster than the current waveform increase. Since the channel expansion speed is almost the same for those two cases, the difference in the spark channel resistance comes mainly from the difference in the electrical resistivity of the spark channel. Indeed, the electrical resistivity for case “B” is calculated to be twice that of case “A” at the time of the maximum channel expansion speed. The plasma temperatures for cases “A” and “B” are roughly estimated as 26,000 K and 39,000 K, respectively, by using the well-known Spitzer resistivity model [30]. This result implies that temporal variation of the spark channel resistance during Joule heating should not be ignored in the calculation of the power absorbed in the spark channel.

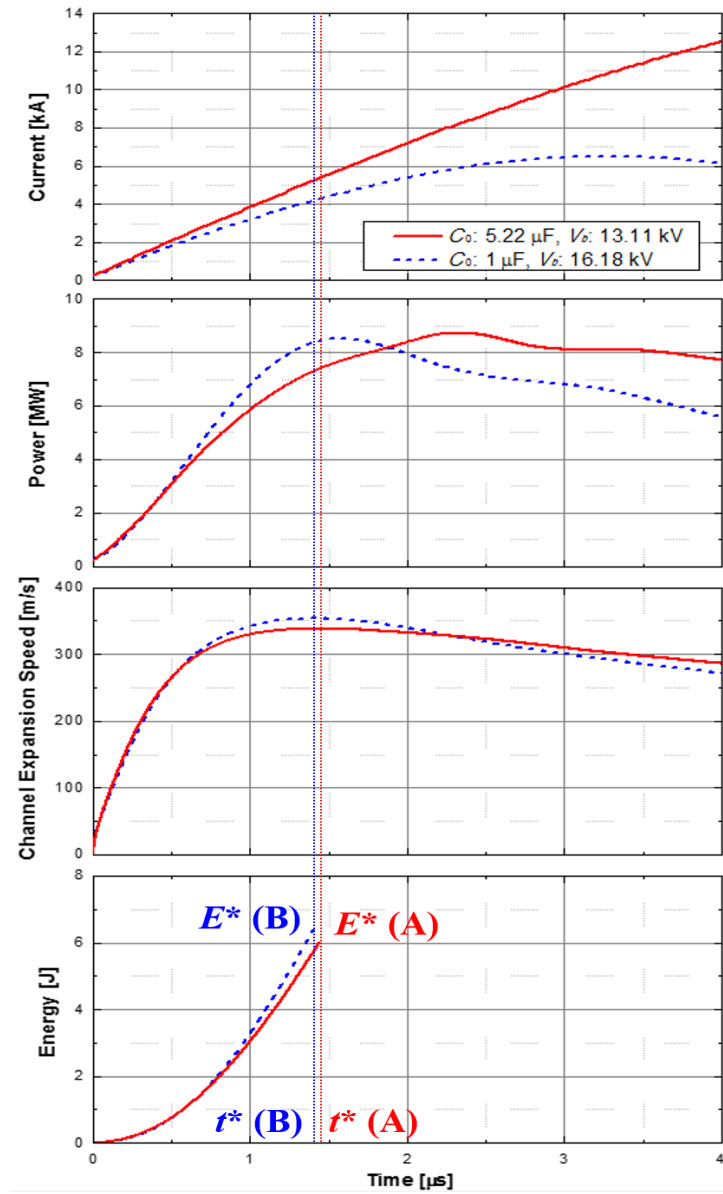


Figure 4.10 Comparison of the current, power, channel expansion speed and energy absorption in the spark channel (E^*) in two different experimental conditions with similar peak pressures (A: $C_0 = 5.22 \mu\text{F}$, $V_b = 13.11 \text{ kV}$; B: $C_0 = 1 \mu\text{F}$, $V_b = 16.18 \text{ kV}$). The calculated value of E^* for the two cases are similar to be $\sim 6 \text{ J}$.

Chapter 5 Analysis for Efficient Generation of Strong Shock Waves

5.1 Energy Efficiency for Shock Wave Formation

Figure 5.1 shows the typical waveforms of the voltage and the current in underwater electrical discharge. The initial charging voltage (V_0) decreases gradually, and the applied voltage across the water gap reaches the breakdown voltage (V_b). When the breakdown voltage is applied across the water gap, the spark channel is formed between the water gap with drastic voltage drop and current rising. After the breakdown, the formed spark channel expands radially and then the shock wave is formed.

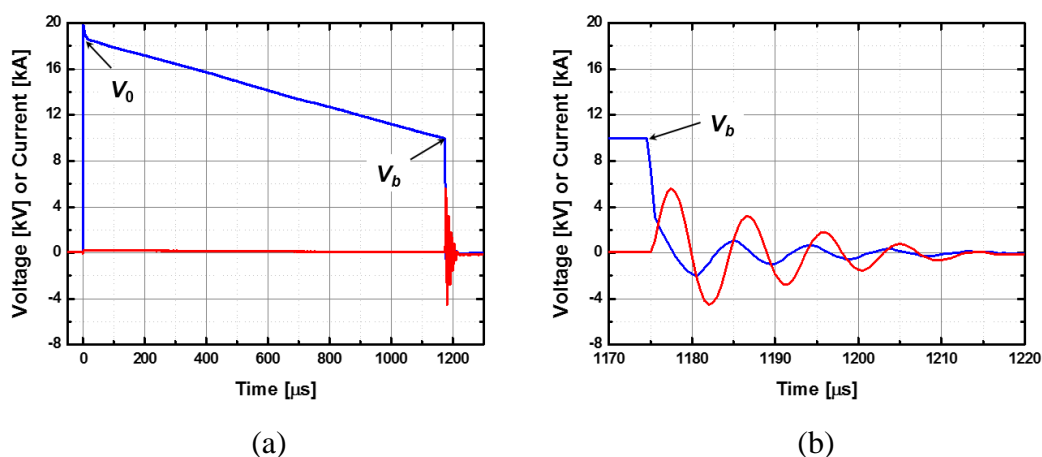


Figure 5.1 Typical waveforms of voltage and current: (a) full scale, (b) specific scale after the breakdown.

For the shock wave formation, the energy flow proceeds in two stages: (a) pre-breakdown, (b) after breakdown. The initial energy stored in the capacitor is defined as follows,

$$E_0 = \frac{1}{2} C_0 V_o^2. \quad (5.1)$$

During the pre-breakdown phase, the Joule heating power by the conduction current flowing through the water heats the water and generates the gas bubble. After the pre-breakdown process is completed, the energy stored in the capacitor is defined as follows,

$$E_b = \frac{1}{2} C_0 V_b^2. \quad (5.2)$$

This energy is injected to the spark channel after the breakdown. In previous researches, the energy E_b is a dominant parameter to determine the peak pressure. The energy efficiency for shock wave formation is expressed as follows from the point of view of the previous researches,

$$\eta_1 = \frac{E_b}{E_0}. \quad (5.3)$$

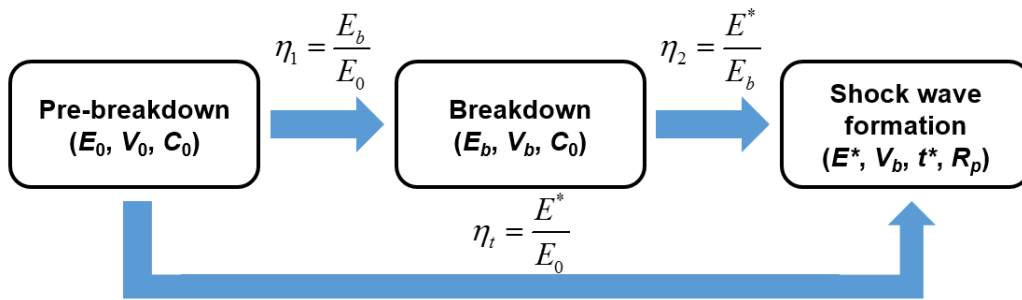


Figure 5.2 Energy efficiency for shock wave formation with considering the mechanism of the shock wave formation.

However, all the energy stored in the capacitor at breakdown does not contribute to the shock wave formation as discussed in Chapter 4. The energy absorbed during the acceleration phase of the spark channel (E^*) is a critical parameter.

$$E^* = \int_0^{t^*} P(t)dt = \int_0^{t^*} i^2(t) \times R_p(t)dt . \quad (5.4)$$

The slope of current and the current waveform at early stage of the discharge can be written as follows,

$$\left. \frac{dI}{dt} \right|_{t=0} = \frac{V_b}{L}, \quad i(t) = \frac{V_b}{L} t . \quad (5.5)$$

Consequently, E^* is defined as follows,

$$E^* = \int_0^{t^*} \left(\frac{V_b}{L} t \right)^2 \times R_p(t)dt . \quad (5.6)$$

The energy efficiency after the breakdown is expressed as follows,

$$\eta_2 = \frac{E^*}{E_b} . \quad (5.7)$$

As a result, the total energy efficiency is given by

$$\eta_t = \eta_1 \eta_2 = \frac{E_b}{E_0} \frac{E^*}{E_b} = \frac{E^*}{E_0} . \quad (5.8)$$

The total energy efficiency for the shock wave formation is derived from two processes. For the first phase as pre-breakdown, the amount of the energy, which is controlled by the electrode geometry and applied voltage, is important to generate the gas bubble and the streamer. And for the second phase as after breakdown, the time dependent energy transfer to the spark channel is important. Therefore, it is necessary to understand the time-varying energy transfer trend after the breakdown as well as the energy consumption for the pre-breakdown phase.

5.2 Effect of Initial Resistance of Spark Channel

The pre-breakdown process determines the initial condition of the spark channel, represented by the initial resistance of the spark channel at the breakdown, which may influence plasma resistance evolution after breakdown. If the resistance of the spark channel is $R(t)=R_0 \times r_p(t)$, Eq. (5.6) is modified as follows,

$$E^* = \left(\frac{V_b}{L}\right)^2 R_0 \int_0^{t^*} t^2 \times r_p(t) dt. \quad (5.9)$$

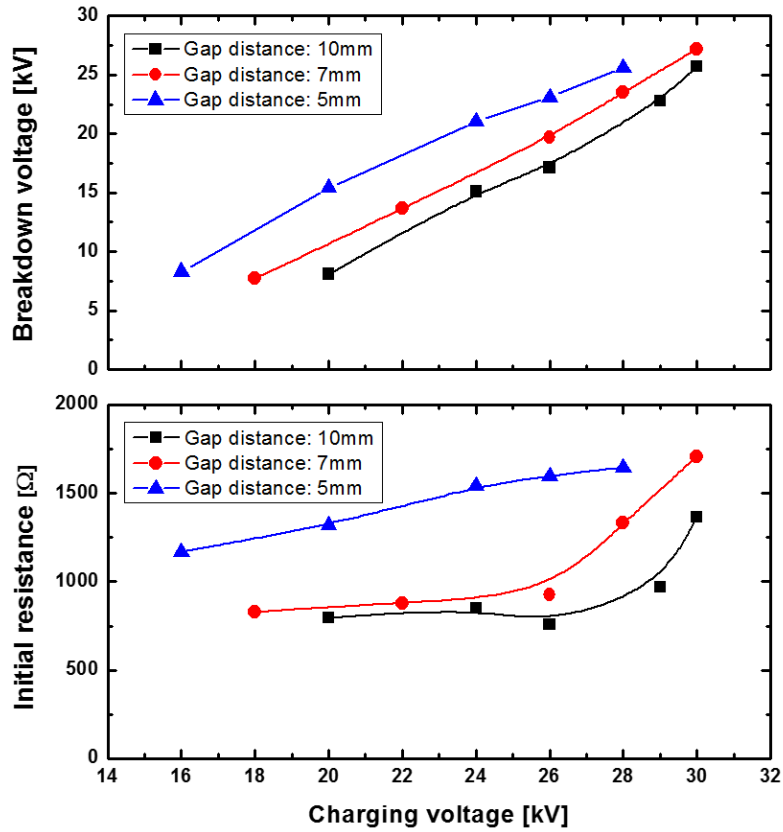


Figure 5.3 Comparison of the breakdown voltage and initial resistance of the spark channel with various charging voltages and gap distances under the capacitance of 1 μ F.

As ignoring the time dependent term in Eq. (5.9) and considering the fixed inductance of the circuit, it is estimated that E^* and the peak pressure is simply proportional to the value of $V_b^2 \times R_0$. In other words, the condition of high initial resistance of the spark channel and high breakdown voltage applied at the spark channel leads to the strong peak pressure. Figure 5.3 shows the breakdown voltage and initial resistance of the spark channel as increasing charging voltage. The breakdown voltage is higher with shorter gap distance in all of the charging voltage. Whereas, the initial channel resistance of long gap distance is low in low charging voltage regime, but the initial channel resistances converge at specific point. According to this results, the peak pressure of the short gap distance is higher than that of the long gap distance in low charging voltage regime, and the peak pressures of all gap distance is similar in high charging voltage regime. However, Figure 5.4, which shows the peak pressure as increasing $V_b^2 \times R_0$ with three gap distance conditions, is different from the estimation based on Figure 5.3. There is no difference of the peak pressure with gap distance in low $V_b^2 \times R_0$ regime, whereas the peak pressure of short distance is higher than that of the long distance in $V_b^2 \times R_0$ high regime. Therefore, the delivered energy to the spark channel at the breakdown (time of $R = R_0$) have almost no effect on the shock wave formation, and it is important to consider the time dependent energy transfer to the spark channel for determining the peak pressure.

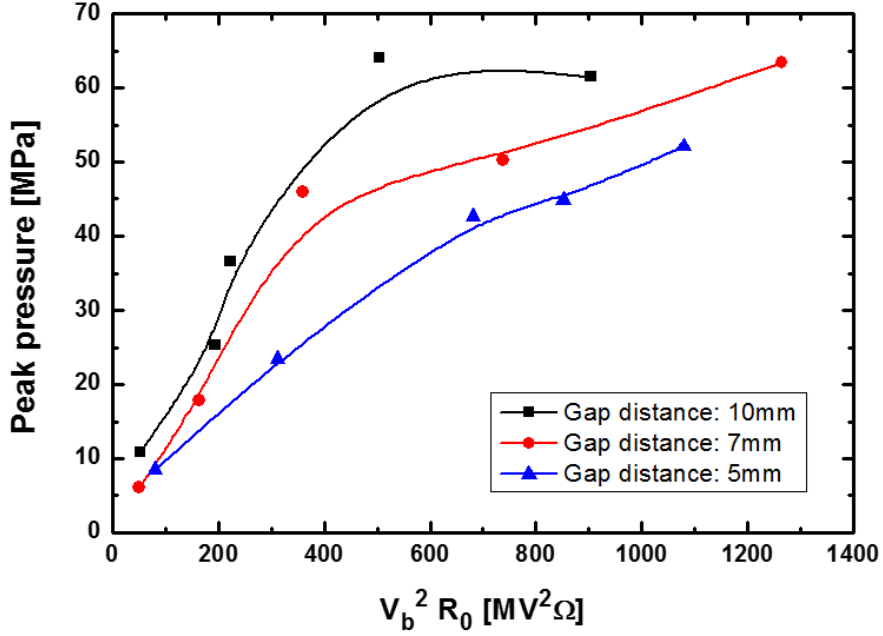


Figure 5.4 Comparison of the peak pressure as increasing $V_b^2 \times R_0$ with various gap distance and the fixed capacitance of 1 μF .

5.3 Correlation of Spark Channel Resistance and E^*

5.3.1 Effects of Spark Channel Resistance on E^*

The temporal power absorption in the spark channel is determined by the spark channel resistance as well as the current flowing in the spark channel. To evaluate the influence of the spark channel resistance on E^* , or equivalently the peak pressure, we calculate the variation of E^* for various shapes of the power absorption profile, which depend on the resistance model, by using

$$P(t) \propto i^2(t) R_{ch}(i) \quad (5.10)$$

where $R_{ch}(i)$ is the spark channel resistance, which is nominally a function of the discharge current [32, 33]. For simplicity, the current waveform is assumed to be a half sine wave with a half period of τ , and the peak power is fixed at the specific value by adjusting the proportionality constant of Eq. (5.10). Then, the power absorption profile is only determined by the resistance model.

The current waveform flowing in the spark channel is expressed as follows,

$$i(t) = \frac{V_b}{L\omega_d} e^{-\beta t} \sin(\omega_d t), \left(\omega_d \sim \frac{1}{\sqrt{LC}}, \beta = \frac{R}{2L} \right). \quad (5.11)$$

Because the shock pressure is formed during the first half-cycle of the oscillating current waveform, the exponential term is ignored in Eq. (5.11). Therefore, the current waveform is expressed as below,

$$i(t) \approx \frac{V_b}{L\omega_d} \sin(\omega_d t). \quad (5.12)$$

The simple resistance model is presented as follows. If the spark channel is fully ionized, the resistivity of the spark channel agrees with Spitzer resistivity. Therefore, the resistivity of the spark channel is described as follows,

$$\rho_e = \frac{1}{\sigma_e} \propto T^{-3/2}. \quad (5.13)$$

And it is assumed that the Joule heating power delivered to the spark channel contributes to increase the temperature of the spark channel because the density of the spark channel is enough. The Joule heating power can be written as below,

$$i^2 R \propto T. \quad (5.14)$$

The simple Spitzer resistance model is obtained from above two equations as follows,

$$i^2 R \propto R^{-2/3} \Rightarrow R \propto i^{-6/5}. \quad (5.15)$$

Besides the Spitzer resistance model, there are numerous established

Table 5.1 Comparison of the resistance models of the spark channel [32, 33]

Model	Equation	Features
Arc welder's ansatz	$R_p \propto i^{-1}$	- Experimental equation
Rompe-Weizel	$R_p \propto \left(\int i^2 \cdot dt \right)^{-0.5}$	- No radiative/thermal losses - Conductivity $\propto T_e$
Spitzer resistivity	$R_p \propto i^{-1.2}$	- Electron-ion collision dominant - Conductivity $\propto T_e^{3/2}$

resistance models for high-current pulsed arc discharges. Among those resistance models, the selected resistance models of the spark channel are summarized in Table 5.1 [32, 33]. Those resistance models of the spark channel are function of current and time-varying power function. The constant resistance model is added on this list of the resistance model.

The delivered power to the spark channel is defined by multiplication of the square of current of Eq. (5.12) and the resistance model. Figure 5.5 (a) shows the arbitrary current waveform plotted by Eq. (5.12), and Figure 5.5 (b) shows the power waveforms calculated from the current waveform in Figure 5.5 (a) with changing the resistance model. In this arbitrary power waveform, the peak power is determined by the capacitance and the breakdown voltage, and the half period of the power waveform is determined by the capacitance at the fixed inductance of a capacitive pulsed power system.

Figure 5.6 shows the five calculated E^* with respect to four resistance models of the Figure 5.5 (b), including experimental result as increasing the half period of the power waveform. The increase of the half period means the increase of the capacitance because the half period is $\pi\sqrt{LC}$ with constant L . Note that increasing the half period at a fixed peak power is roughly equivalent to increasing

the capacitance with decreasing the breakdown voltage. In constant resistance model, the E^* increases is seen to increase gradually with increasing half period. However, this tendency is not observed in the experiments and other models. Therefore, the constant resistance model seems not to be applicable for the modeling of a pulsed spark discharge in water. In the case of the arc welder's ansatz model, the power is proportional to the current i.e. $P(t) \sim i(t)$ because the resistance is inversely proportional to the current i.e. $R_{ch}(i) \sim i(t)^{-1}$. E^* also increases with increasing half period, but its slope becomes more gentle with increasing half period. For the Weizel-Rompe resistance model, we observe that E^* increases with increasing half period for low values of half period similar to other models, but it begins to decrease with half period for $\pi\sqrt{LC} > \sim 4 \mu s$. In the case of the Spitzer resistance model, the value of E^* is very similar to the experimental result. Meanwhile, experiments carried out with the identical peak

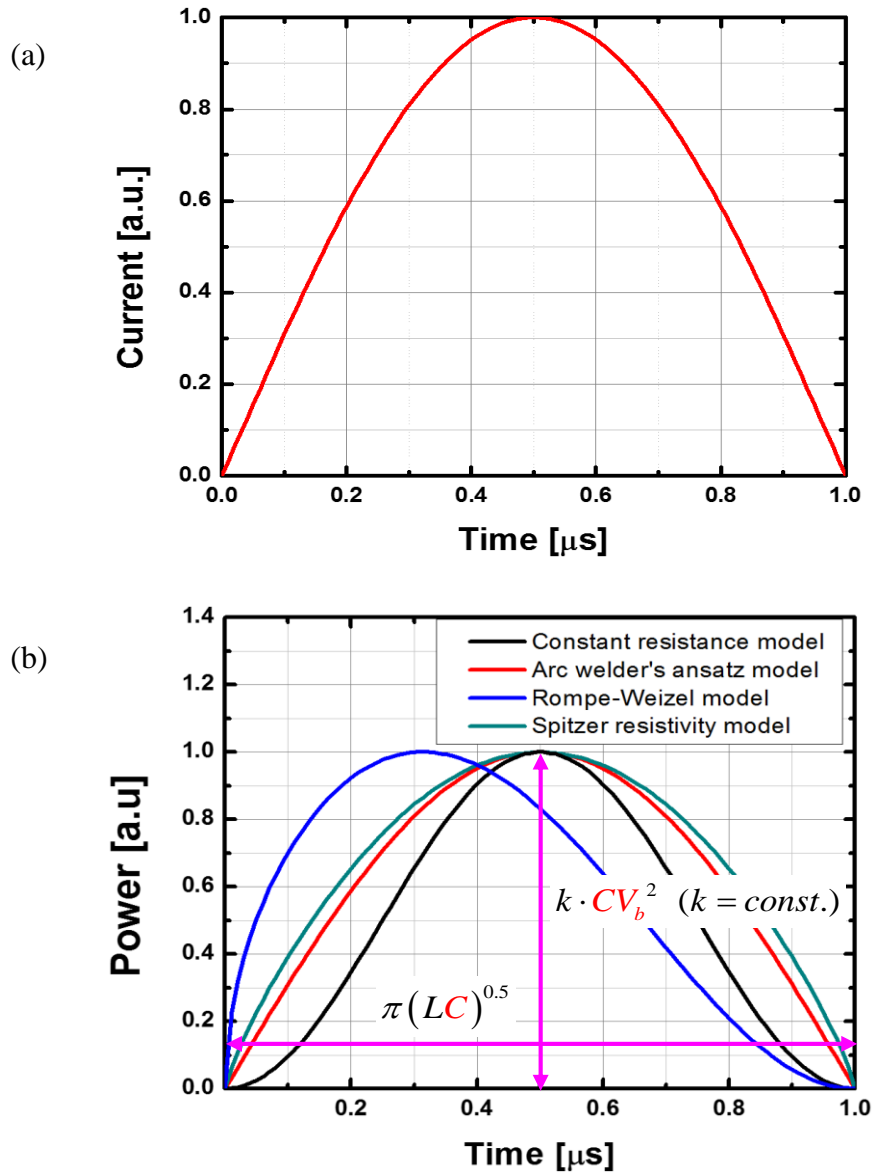


Figure 5.5 (a) Arbitrary current waveform obtained from equation (5.6), (b) Comparison of the power waveform depending on the resistance model with identical arbitrary current waveform of (a).

power of 8 MW but different half period values show that E^* is hardly affected by half period within our experimental ranges of 6 ~ 17 μs . This means that the spark channel resistance obeys a model different from either the arc welder's ansatz model or the Weizel-Rompe model. Practically, the experimental result shown in Figure 5.6 indicates that the higher peak pressure cannot be achieved by increasing the capacitance with a lower charging voltage.

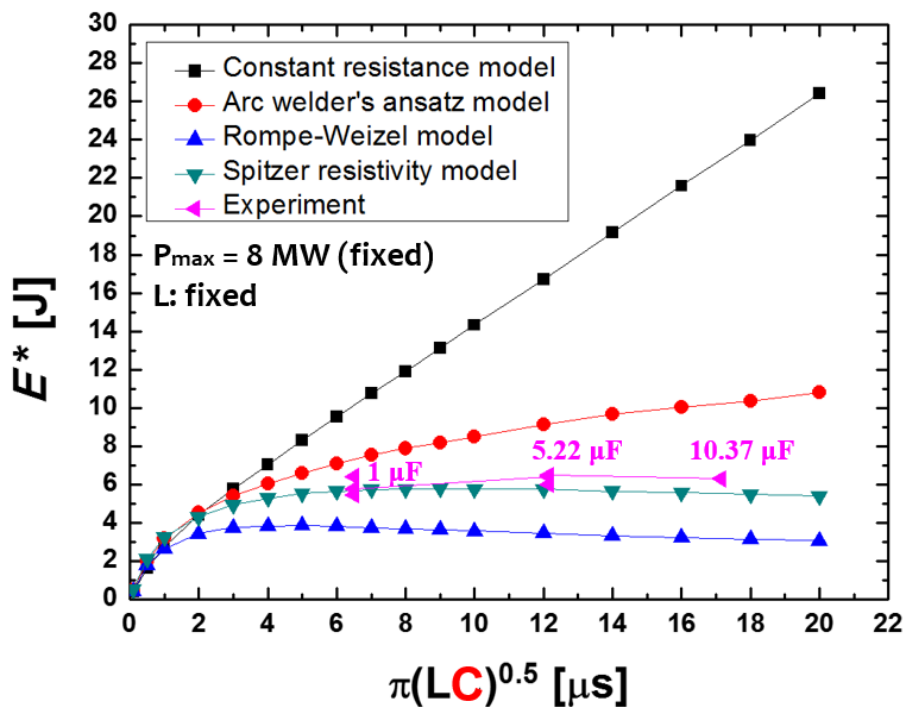


Figure 5.6 Comparison of the energy absorbed in the spark channel until the channel expansion speed reaches the maximum value between experiment and the resistance models with changing the capacitance.

5.3.2 Limitation of Resistance Model

In Figure 5.6, the experiment results of E^* is correspond to the results of the calculated E^* from the Spitzer resistance model. However, the Spitzer resistance model does not accurately describe the experiments.

Figure 5.7 shows that the power waveform with Spitzer resistance model is compared with the experimental result until the time of maximum channel expansion speed. Although E^* is similar between the calculation by Spitzer resistance model and the experiment, the shape of the power and the time of maximum channel expansion speed are different. In experiment, the power of the Spitzer resistance model increases faster than that of the experiment. And the time of the maximum power and t^* of the Spitzer resistance model appear faster than those of the experiment.

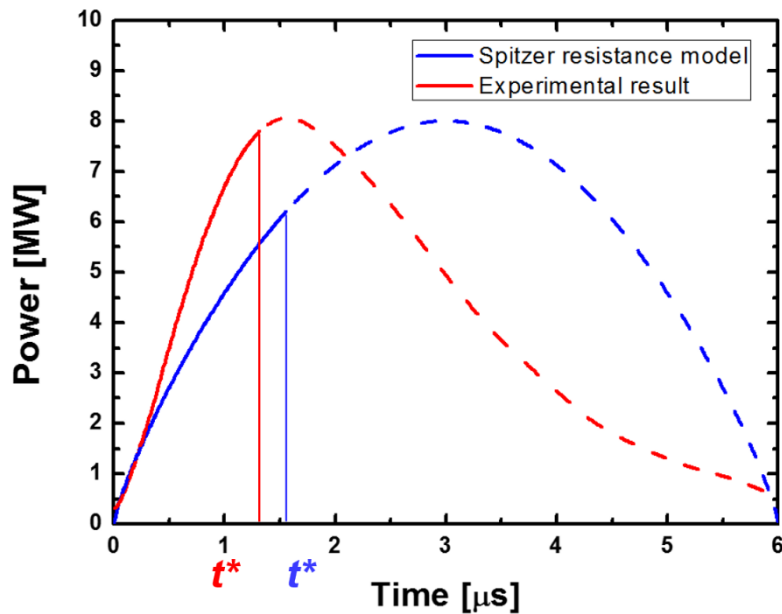


Figure 5.7 Comparison of the power waveform between experiment and the resistance model with capacitance of $5.22 \mu\text{F}$, maximum power of 8MW.

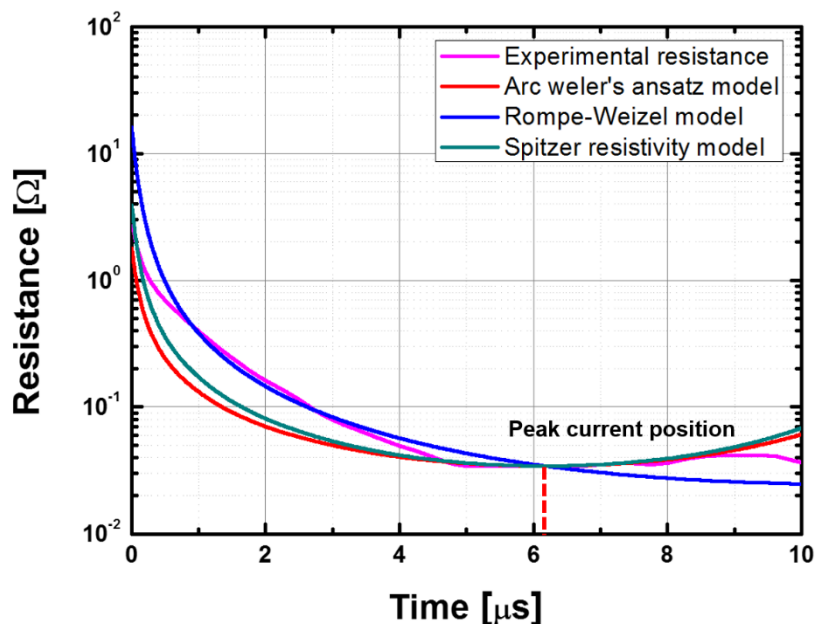


Figure 5.8 Comparison of the resistance between experiment and various resistance model with capacitance of 5.22 μF , maximum power of 8MW.

The resistance of the experiment is compared with various resistance models presented in previous section, as shown in Figure 5.8. All of the resistances calculated by resistance model match with the resistance of the experiment at the time of peak current (approximately $t = 6.1 \mu\text{s}$). The resistance of arc welder's ansatz model or the Spitzer resistance model is lower than the resistance of experiment before 4.3 μs . The resistance of Rompe-Weizel model does not correspond to the resistance experiment within 1 μs . Because the resistance models consider the ion-electron collision, the spark channel is complicated to analyze by the well-known resistance model. Consequentially, the established resistance model has limitation for accurate description of the time-varying resistance in the spark channel. Therefore more accurate model is needed for depicting accurately the resistance of the spark channel in UPSD.

5.3.3 1D MHD Model

In fully ionized plasmas, the motion of the electron is governed by Coulomb collision with ion in plasma. The resistance models summarized in Table 5.1 considered only the ion-electron collision for determining the electrical conductivity of the plasma. However, the spark channel described in this dissertation is not fully ionized, but partially ionized. Therefore, the electrical conductivity of this spark channel is calculated by considering the ion-electron collision as well as ion-neutral particle collision. Figure 5.9 shows the calculated electrical conductivity of the spark channel in water with temperature and mass density ratio of the spark channel. The electrical conductivity increases rapidly from 10^2 S/m to 10^4 S/m until 20,000 K. And the electrical conductivity decreases

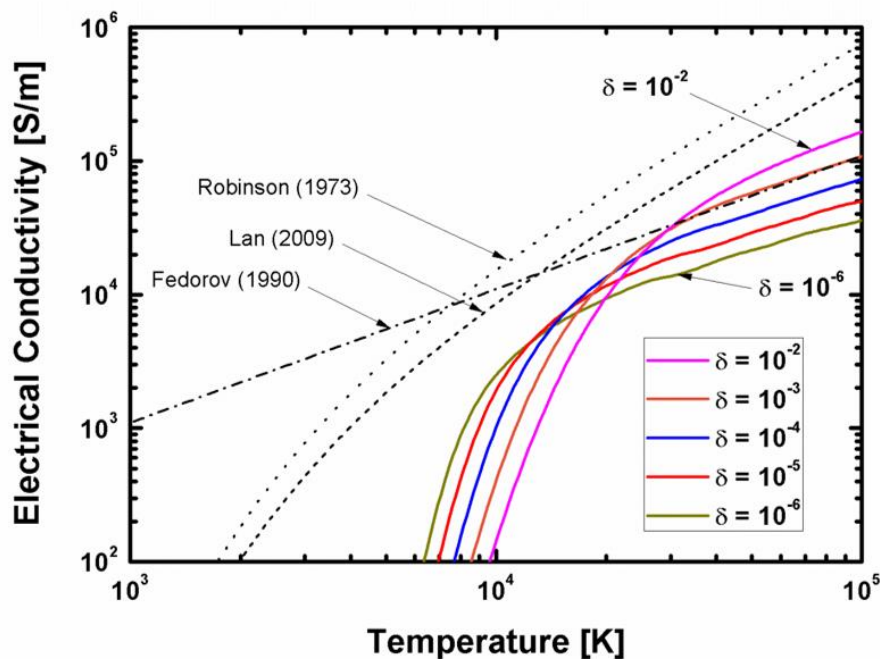


Figure 5.9 Electrical conductivities of water plasma with temperature and mass density ratio (δ = plasma density/water density at STP) [34].

as mass density ratio increases at lower fixed temperatures. The Fedorov's electrical conductivity considered only electron-ion collision. For this reason, the Fedorov's electrical conductivity seems to agree with the electrical conductivity, which calculated by considering the ion-neutral collision, above 30,000 K.

To acquire the accurate resistance of the spark channel and understand the physical mechanism for shock wave generation by underwater spark discharge, a self-consistent model is developed [5]. The UPSD is expressed simply by a RLC circuit and the equivalent circuit is described as shown in Figure 5.10. The circuit parameters of the spark channel (L_p and R_p), and the external circuit parameters influence each other.

The equivalent circuit is governed by the equation as below

$$\left(L_0 + L_c + L_p(t) \right) \frac{dI(t)}{dt} + \left(R_0 + R_c + R_p(t) + \frac{dL_p(t)}{dt} \right) I(t) + \frac{1}{C_0} \int_0^t I(\tau) d\tau = V_b. \quad (5.16)$$

The time-varying resistance and inductance of the spark channel can be written as follows

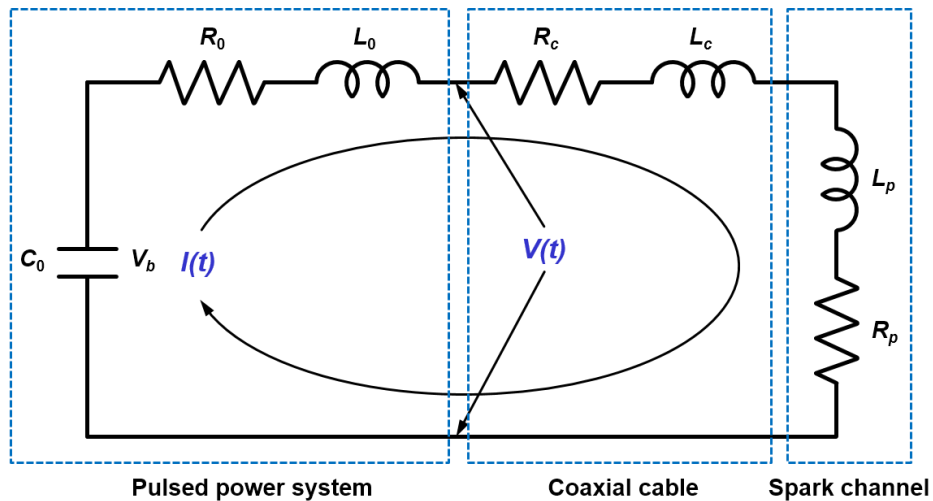


Figure 5.10 Equivalent circuit of the UPSD system [6].

$$R_p(t) = \frac{l}{\int_0^{a(t)} \sigma(r) \cdot 2\pi r \cdot dr}, \quad (5.17)$$

$$L_p(t) = \frac{\mu_0 l}{2\pi} \left[\ln \left(\frac{2l}{a(t)} \right) - \frac{3}{4} \right], \quad (5.18)$$

respectively. In Eqs. (5.17) and (5.18), a fixed length of l is the gap distance and the channel radius $a(t)$, the electrical conductivity $\sigma(r)$ is obtained by solving the equations as follows:

$$\rho \frac{du}{dt} = -\frac{\partial p}{\partial r} - \sigma E_z B_\theta \quad (\text{Momentum equation}); \quad (5.19)$$

$$\frac{dr}{dt} = u \quad (\text{Equation of motion}); \quad (5.20)$$

$$\left(\frac{\partial \varepsilon}{\partial T} \right)_\rho \frac{dT}{dt} + \left[p + \left(\frac{\partial \varepsilon}{\partial \rho^{-1}} \right)_T \right] \frac{d\rho^{-1}}{dt} = \rho^{-1} \left[Q_J + \frac{1}{r} \frac{\partial}{\partial r} \left(r \kappa_c \frac{\partial T}{\partial r} \right) - Q_R \right]$$

$$(\text{Energy conservation}); \quad (5.21)$$

$$\frac{1}{r} \frac{\partial}{\partial r} (r B_\theta) = \mu_0 \sigma E_z \quad (\text{Ampere's law}); \quad (5.22)$$

$$E_z = \frac{I}{\int_0^a \sigma(r) \cdot 2\pi r \cdot dr} \quad (\text{Ohm's law}); \quad (5.23)$$

$$p = p(\rho, T) \quad (\text{Equation of state}); \quad (5.24)$$

$$Q_J = \sigma E_z^2 \quad (\text{Joule heating}); \quad (5.25)$$

$$Q_R = \sigma_s \frac{T^4}{l_p} \quad (\text{Radiation loss}); \quad (5.26)$$

The resistance and inductance of the spark channel is obtained by using the time-

varying channel radius and electrical conductivity obtained from above equations. Those updated resistance and inductance produce the updated electrical current and voltage. The Joule heating power is calculated from updated electrical current and voltage. In this manner, time-varying current, voltage and resistance is obtained and the calculated voltage, current and resistance is well suited to the experimental results as shown in Figure 5.11.

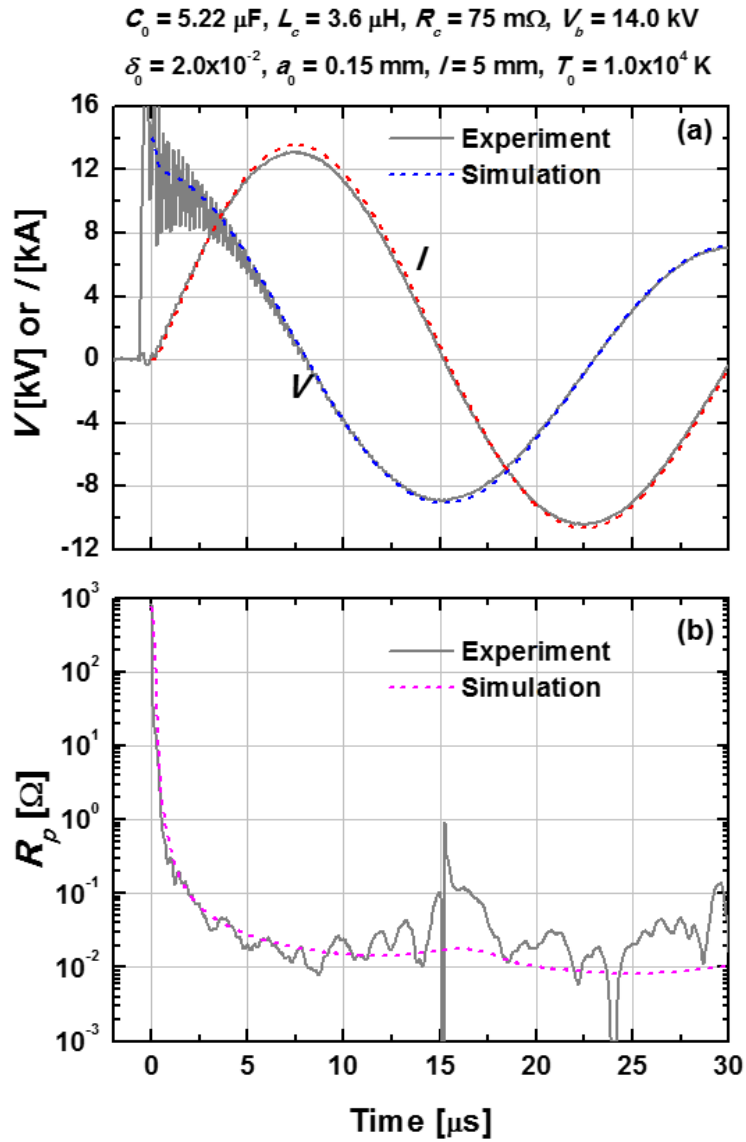


Figure 5.11 Comparison of (a) the voltage, current, and pressure waveforms (b) the calculated spark channel resistance between experiment and simulation with the charging voltage of 14 kV.

5.4 Effects of Operating Parameters on Peak Pressure

5.4.1 Effect of Capacitance

To understand the effect of the capacitance of the pulse system on the peak pressure, the discharge experiments and simulation are carried out at the fixed breakdown voltage of 14kV and gap distance of 5 mm. In simulation, the capacitance varies from 2 nF to 50 μF . And the three capacitance value with 0.1, 1, 5.22 μF are used in the experiments.

Figure 5.12 shows the comparison of the calculated E^* with the measured and simulated peak pressure by varying the capacitance. The peak pressure seems to saturate after 1 μF in both cases of experiment and simulation. To investigate the reason of the peak pressure saturation, E^* is calculated by 1D MHD model. As shown in Figure 5.12, the tendency of E^* is analogous to the tendency of the peak

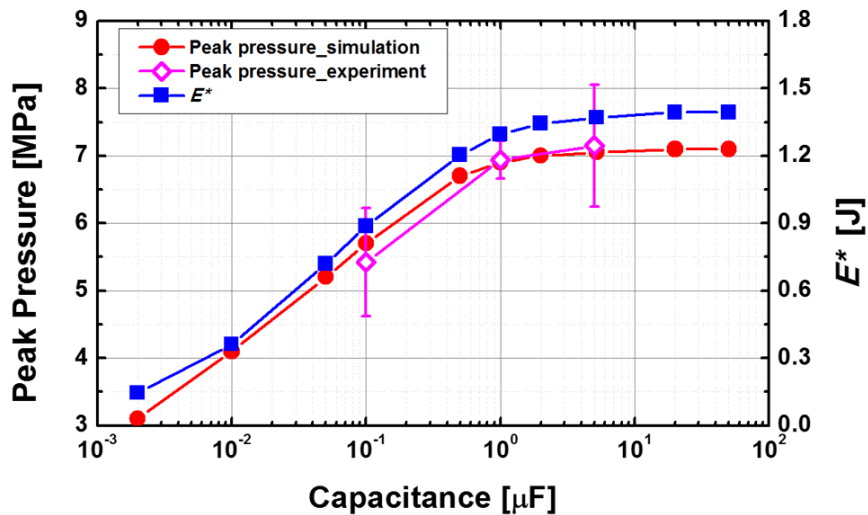


Figure 5.12 Comparison of the E^* and peak pressure versus various capacitance in identical charging voltage of 14 kV.

pressure. As stated in Chap. 4, E^* is a dominant parameter to determine the peak pressure, and the peak pressure is proportional to E^* . Therefore, the peak pressure seems to saturate above 1 μF in the experiment because E^* tends to saturate above 1 μF .

To investigate the reason of saturation of E^* above 1 μF , the power waveforms are compared with various capacitances until the channel expansion speed reaches the maximum value, as shown in Figure 5.13. In low capacitance regime, the time t^* almost approaches the half period of the power waveform. For this reason, as increasing the capacitance in low capacitance regime, the half period of the power waveform and the energy integrated the power until t^* increase. Therefore, E^* corresponds to the tendency of the energy integrated the power until t^* . In high capacitance regime, however, time t^* appears below the half period of the power waveform and time t^* tends to saturate. Furthermore, the power waveforms have no difference with respect to the capacitance until t^* . Because the slope of the power is determined by the breakdown voltage and the inductance at

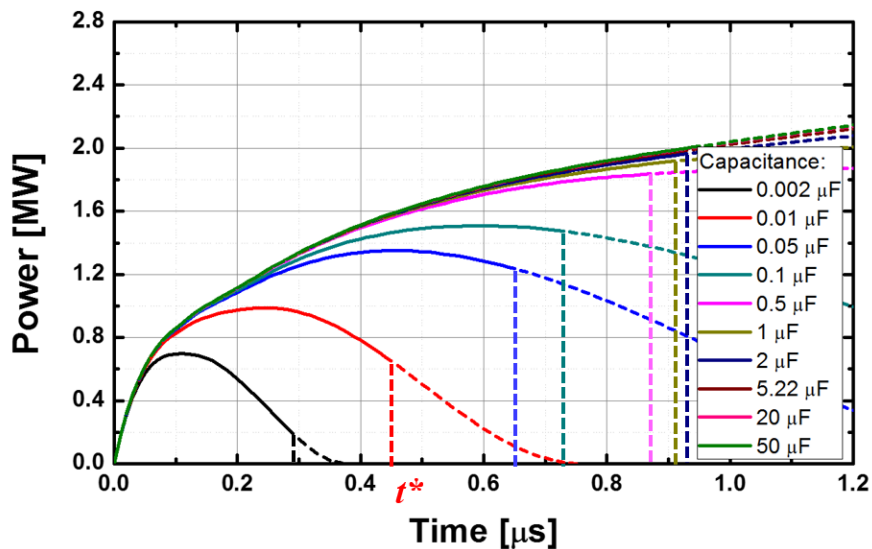


Figure 5.13 Comparison of the power waveforms until t^* with various capacitance.

early stage of discharge, E^* is almost similar irrespective of the capacitance. As a result, there is the optimum capacitance value for the maximum peak pressure at the fixed breakdown voltage and gap distance.

5.4.2 Effect of Breakdown Voltage

Figure 5.14 shows the dependency of the peak pressure on the breakdown voltage and gap distance at the fixed capacitance of $5.22 \mu\text{F}$. The simulation results are almost correspond to the experimental results. As increasing the breakdown voltage, the peak pressure increases in the condition of the identical capacitance

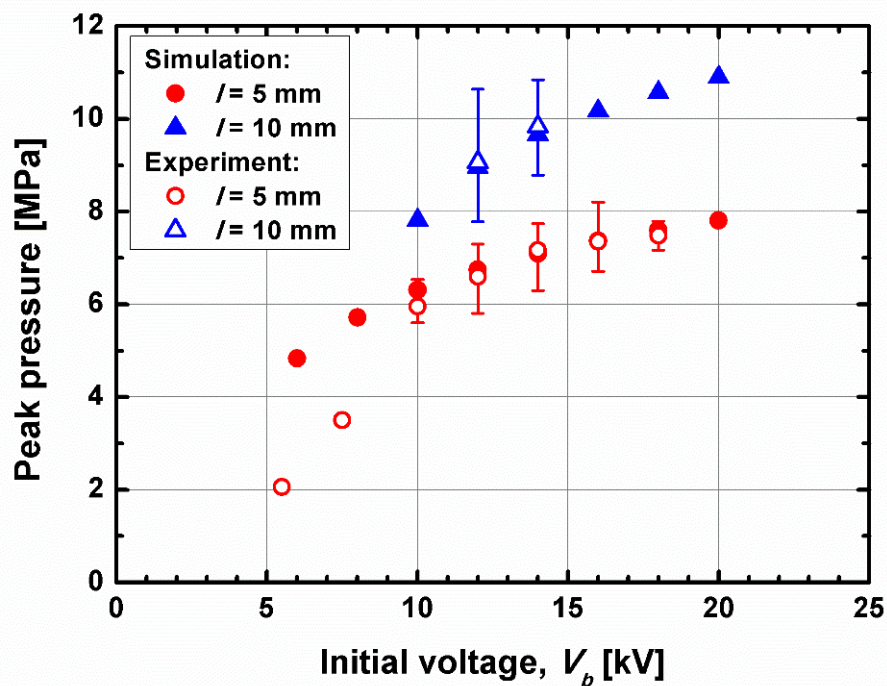


Figure 5.14 Comparison of the peak pressure with changing the breakdown voltage and gap distance in identical capacitance.

and gap distance.

To investigate the reason of this correlation of the peak pressure with the breakdown voltage, E^* and t^* are calculated and compared with various breakdown voltages at the fixed capacitance and gap distance, as shown in Figure 5.14. As stated in Sec. 5.3.1 (Figure 5.5 (b)), the maximum value of the power is determined by the breakdown voltage at the condition of fixed capacitance. In Figure 5.15 (b), t^* seems to saturate with increasing the maximum value of the power in the condition of identical capacitance. Although t^* tends to saturate, E^* increases because the maximum value of the power increases with identical half period of the power.

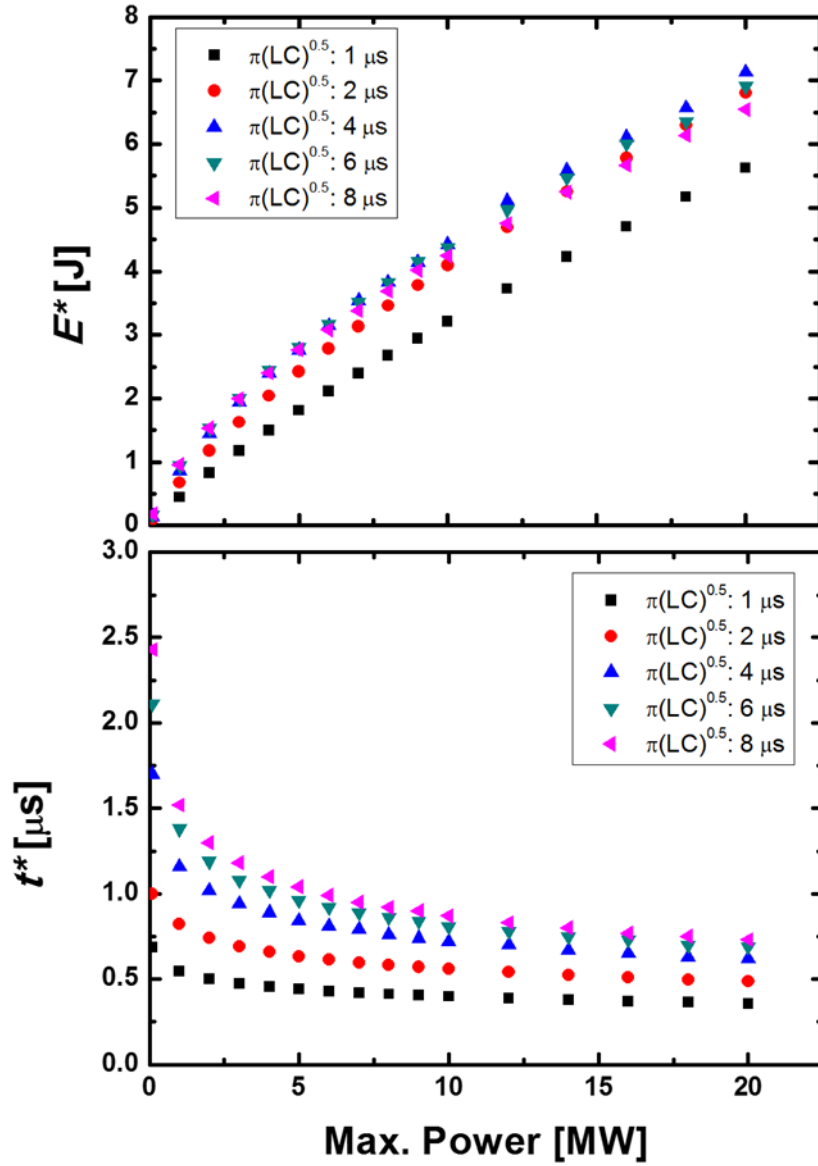


Figure 5.15 Comparison of E^* and t^* with various maximum power (breakdown voltage) in identical capacitance.

5.4.3 Effect of Gap Distance

In Figure 5.13, the peak pressure of long gap distance is larger than that of the short gap distance. The tendency of E^* with changing the gap distance correspond to the tendency of the peak pressure. In condition of fixed capacitance and breakdown voltage, the current waveforms are identical, irrespective of the gap distance. As a result, the power waveform is determined by the spark channel resistance. Because the spark channel resistance is higher with longer gap distance, the power rising rate is faster with longer gap distance. Therefore, in case of the capacitance above 1 μF , E^* increases with increasing the gap distance because t^* tends to saturate.

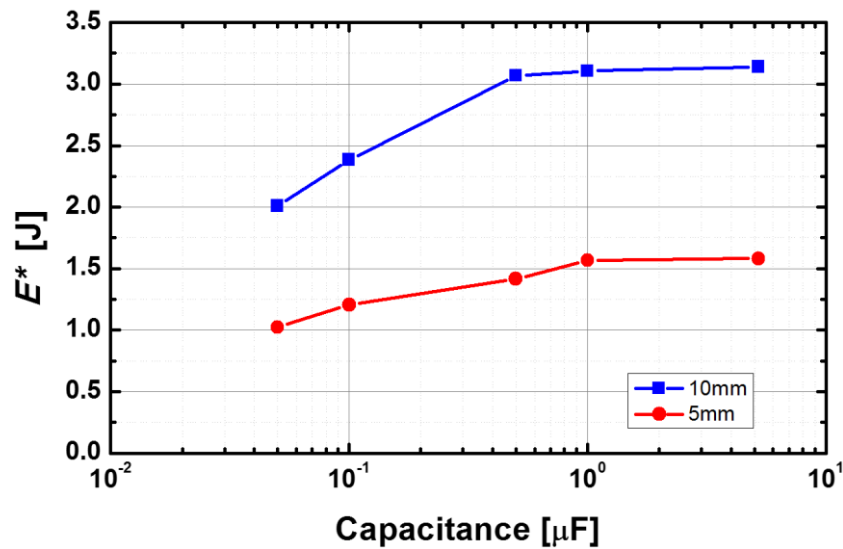


Figure 5.16 Comparison of E^* with two gap distance and various capacitances at the fixed breakdown voltage of 20 kV.

Chapter 6 Conclusion

The objective of this research was to investigate the mechanism of the UPSD and find the critical parameter for obtaining the strong shock wave (or high peak pressure) in UPSD, because the treatment efficiency is generally proportional to the strength of the shock wave.

The phenomenon before the breakdown proceeds in four stage: (i) water heating, (ii) gas bubble generation and expansion, (iii) electron avalanche, and (iv) streamer propagation to the cathode. During the pre-breakdown phase, the energy is consumed for preparing the plasma channel formation and this energy does not contribute to the spark channel expansion and shock wave formation after the breakdown. To reduce this energy, it is effective to make the narrow anode exposure area because the energy for water heating, which occupy a large portion of the energy consumed for the pre-breakdown phase, decreases.

The shock wave formation in UPSD can be understood by the fundamental mechanism based on the shock wave generated by an accelerating piston. The shock wave is formed by the accumulation of the compression waves until the spark channel expansion speed reaches the maximum value of the speed. Therefore, the delivered energy to the spark channel during the accelerating phase of the spark channel (E^*) is regarded as a critical parameter to determine the peak pressure. To verify this hypothesis, the experiments are carried out with various charging voltages and capacitances in the condition of identical electrodes geometry. As a result, the peak pressure is not consistent by the energy stored in the capacitor at breakdown (E_b) but the peak pressure is proportional to E^* .

The resistance of the spark channel is important to determine E^* . To investigate the effect of the channel resistance on E^* , the experiment results compare with calculated E^* with various resistance models. Consequently, the resistance is a time-varying waveform and the variation of the resistance at early stage of discharge affects E^* .

There is a difficult to define the channel resistance accurately as function of current, because the channel resistance and the delivered power to the spark channel mutually interact. For this reason, the self-consistent model is constructed. By using this model, the optimum condition of the strong shock wave formation is investigated.

To generate the strong shock wave, it is important to increase the energy absorbed to the spark channel at early stage of the discharge. It is possible that this energy is adjusted effectively by selecting the appropriate circuit parameters such as the capacitance, breakdown voltage and gap distance. As increasing the capacitance with fixed breakdown voltage and gap distance, the peak pressure and E^* tends to saturate above specific capacitance. In case of variable breakdown voltage with fixed capacitance and gap distance, the peak pressure and E^* increase with increasing the breakdown voltage because the power rising rate is faster with higher breakdown voltage. And the longer gap distance make the strong peak pressure at the fixed capacitance and breakdown voltage, because the long gap distance make the initial resistance of the spark channel is high and it leads to increase the rising rate of the power, although the problem of the increasing breakdown voltage with increasing the gap distance.

This research provides the better understanding of the shock wave formation mechanism and the fundamental design parameters for obtaining the strong shock wave.

References

- [1] A. Yamatake, D. M. Angeloni, S. E. Dickson, M. B. Emelko, K. Yasuoka and J. S. Chang, "Characteristics of pulsed arc electrohydraulic discharge for eccentric electrode cylindrical reactor using phosphate-buffered saline water," *Jap. J. Appl. Phys.* **45**(10B), 8298 (2006)
- [2] P. Bruggeman and C. Leys, "Non-thermal plasmas in and in contact with liquids," *J. Phys. D: Appl. Phys.* **42**, 053001 (2009).
- [3] F. Jonmni, F. Aitken and A. Denat, "Experimental investigation of transient pressure waves produced in dielectric liquids," *J. Acoust. Soc. Am.* **107**(3), 1203 (2000).
- [4] L. H. Fry, P. Adair Jr. and R. Williams, "Long life sparker for pulse powered underwater acoustic transducer," 12th IEEE International Pulsed Power Conference, Monterey, California, USA, (1999).
- [5] P. Sunka, "Pulse electrical discharges in water and their applications," *Phys. Plasmas* **8**(5), 2587 (2001).
- [6] K. J. Chung, S. G. Lee, Y. S. Hwang and C. Y. Kim, "Modeling of pulsed spark discharge in water and its application to well cleaning," *Curr. Appl. Phys.* **15**(9), 977 (2015).
- [7] A. H. Sharbaugh, J. C. Devins, S. J. Rzed, "Progress in the field of electric breakdown in dielectric liquids," *IEEE Trans. Electr. Insul.* **13**(4), 249 (1978).
- [8] R. Laenen, T. Roth, A. Laubereau, "Novel precursors of solvated electrons in water: evidence for a charge transfer process," *Phys. Rev. Lett.* **85**(1), 50 (2000).

- [9] G. Touya, T. Reess, L. Pecastaing, A. Gibert, and P. Domens, "Development of subsonic electrical discharges in water and measurements of the associated pressure waves," *J. Phys. D: Appl. Phys.* **39**, 5236 (2006).
- [10] J. F. Kolb, R. P. Joshi, S. Xiao, and K. H. Schoenbach, "Streamers in water and other dielectric liquids," *J. Phys. D: Appl. Phys.* **41**(23), 234007 (2008).
- [11] B. R. Locke, M. Sato, P. Sunka, M. R. Hoffmann and J. S. Chang, "Electrohydraulic discharge and nonthermal plasma for water treatment," *Ind. Eng. Chem. Res.* **45**, 882 (2006).
- [12] Y. Yang, "Plasma discharge in water and its application for industrial cooling water treatment," Ph.D. dissertation, Drexel University, (2011).
- [13] Available at <http://www.imo.org>
- [14] E. Tsolaki and E. Diamadopoulos, "Technologies for ballast water treatment: a review," *J. Chem. Technol. Biotechnol.* **85**, 19 (2010)
- [15] C. Y. Hwang, S. S. Choi, *et al.*, *Plasma ballast water treatment system development: report*, Seoul National University, PBWTS Inc. (USA), (2009).
- [16] C. Y. Hwang, S. W. Jung, Y. S. Hwang and B. C. Cho, "Lethal effects of pulsed high-voltage discharge on marine plankton and *Escherichia coli*," *Water Air Soil Pollut* **213**, 161 (2010).
- [17] K. J. Chung, S. G. Lee, J. J. Dang, G. H. Choi, Y. S. Hwang, C. Y. Kim and Y. J. Park, "Feasibility study for the cleaning of well screens using high-voltage pulsed discharge," *J. Eng. Geo.* **23**(1), 29 (2013) (in Korean).
- [18] E. A. Martin, "Experimental investigation of a high-energy density, high-pressure arc plasma," *J. Appl. Phys.* **31**(2), 255 (1960).

- [19] D. D. Caulfield, "Predicting sonic pulse shapes of underwater spark discharges," *Deep Sea Research* **9**, 339 (1962).
- [20] W. J. Guman and B. G. Humphrey, Jr., *Studies on an electric discharge underwater sound source: Final report* Fairchild Hiller Corporation, Republic Aviation Division, New York, (1968).
- [21] J. W. Mackersie, I. V. Timoshkin and S. J. MacGregor, "Generation of high-power ultrasound by spark discharges in water," *IEEE Trans. Plasma Sci.* **33**(5), 1715 (2005).
- [22] I. V. Timoshkin, R. A. Fouracre, M. J. Given and S. J. MacGregor, "Hydrodynamic modelling of transient cavities in fluids generated by high voltage spark discharges," *J. Phys. D: Appl. Phys.* **39**(22), 4808 (2006).
- [23] L. D. Landau and E. M. Lifshitz, *Fluid mechanics*, Butterworth-Heinemann, Oxford, (1987).
- [24] Y. B. Zel'dovich and Y. P. Raizer, *Physics of Shock Waves and High-temperature Hydrodynamic Phenomena*, Dover Publications, New York, (2002).
- [25] M. J. Mann, "One-dimensional shock wave formation by an accelerating piston," Ph.D. dissertation, The Ohio State University, (1970).
- [26] Y. B. Zel'dovich, "Theory of shock waves and introduction to gas dynamics," AN SSSR, INSTITUT KHT14ICHESKOY FIZIKI (RUSSIAN) (1946).
- [27] L. K. Warne, R. E. Jorgenson and J. M. Lehr, *Resistance of a water spark: Sandia report*, Sandia National Laboratories, (2005).
- [28] S. I. Braginskii, "Theory of the development of a spark channel," *Sov. Physics - JEPT* **34**(7), 1068 (1958).

- [29] V. V. Shamko and E. V. Krivitskii, "Characteristics of an underwater spark," Soviet Phys.-Tech. Phys. **22**(1), 52 (1977).
- [30] A. I. Ioffe, "Theory of the initial stage of an electrical discharge in water," J. Appl. Mech. and Tech. Phys. **7**(6), 69 (1966).
- [31] L. Spitzer, Jr., *Physics of Fully Ionized Gases*, John Wiley & Sons, New York, (1962).
- [32] T. G. Engel, A. L. Donaldson and M. Kristiansen, "The pulsed discharge arc resistance and its functional behavior," IEEE Trans. Plasma Sci. **17**(2), 323 (1989).
- [33] K. Takaki and H. Akiyama, "The resistance of a high-current pulsed discharge in nitrogen," Jpn. J. Appl. Phys. **40**, 979 (2001).
- [34] K. J. Chung and Y. S. Hwang, "Thermodynamic properties and electrical conductivity of water plasma," Contrib. Plasma Phys. **53**(4-5), 330 (2013).

Abstract in Korean

수중 방전을 통해 발생하는 자외선, 활성화된 라디칼(radical) 및 충격파는 오염 수 처리에 좋은 효율을 보이고 있고, 따라서 수중 방전은 환경 분야에서 많은 관심을 받고 있는 연구 주제이다. 이 중 수중 충격파는 다양한 분야에 응용 가능하며, 침투 속도 또한 빠르기 때문에 높은 응용 효율을 기대할 수 있다. 수중 충격파는 충격파의 압력 크기가 클수록 응용 효과가 상승하기 때문에 충격파의 압력 크기를 높이는 방안에 대한 많은 연구가 진행되어 왔다. 따라서 본 연구는 적은 에너지를 투입하여 강한 충격파 발생시킬 수 있는 방법을 찾기 위해 수중 충격파 발생 원리 및 최적의 운전 조건 등을 제시하고자 한다.

수중 방전은 방전 개시 전과 방전 개시 이후로 나누어 에너지 소모가 이루어 진다. 방전 개시 전 발생하는 에너지 손실은 대부분 전극 사이의 물을 가열하는데 소비되며, 이 에너지 손실은 전극의 구조를 바꿈에 따라 조절 가능하다. 예를 들어 전극 노출 면적을 절반으로 줄이면 물을 가열하는데 소비되는 에너지는 2배 이상 줄어든다. 이 후 실험은 방전 개시 전 에너지 손실을 최대한으로 줄이기 위해 전극 노출 면적을 최소화 하였다.

기존 연구에서는 방전 개시 시점에 축전기에 남아 있는 에너지(E_b)가 충격파의 압력 침투치를 결정한다고 보고 있다. 그러나 기존 연구 결과들은 정전 용량에 관계없이 E_b 에 의해 압력 침투치가 결정된다는 결과도 있고 동일한 E_b 라 할지라도 정전 용량이 크고 방전 개시 전압이 작을수록 압력 침투치가 커진다는 결과도 있다. 이처럼 동일한 E_b 라는 변수를 갖고 상이한 결론을 도출하고 있어, 보다 근본적인 관점에서 수중 방전을 연구할 필요가 있다고 보았다. 이에 본 논문에서는 수중 방전 시 채널 팽창에 의해 발생하는 충격파의 형성 원리를 토대로 충격파의 압력 침투치를 결정하는 인자가 무엇인지를 밝히고자 하였다. 이를 위해 유체 내 가속 피스톤에 의한 충격파 발생 원리에 착안하여 수중 방전에서의 충격파 발생 모델을 설계하였고, 이를

실험적으로 검증하기 위해 동일한 전극 구조하에서 정전 용량(capacitance) 및 충전 전압을 변화시켜가며 수중 방전 실험을 진행하였다.

일반적으로 가속 피스톤에 의해 압축되는 유체 내에서 충격파 형성은 가속 피스톤에 의해 발생한 압축파(compression wave)의 중첩에 의해 발생한다. 이를 수중 방전에도 적용하면, 피스톤 역할을 하는 플라즈마 채널이 팽창하면서 압축파가 발생할 것임을 알 수 있고, 채널 팽창 속도가 최대가 되는 시점까지 발생한 압축파 들만이 충격파 형성에 기여할 것으로 예측할 수 있다. 가속 구간 동안 채널에 전달된 에너지는 수정된 파워 균형식을 이용하여 채널 팽창 속도를 구하고, 최대 채널 팽창 속도에 도달하는 시간까지 채널에 전달된 파워를 적분하여 구하였다. 실험 결과, 가속 구간 동안 채널에 전달된 에너지(E^*)가 압력 침두치를 결정하는 새로운 인자라 볼 수 있었다.

E^* 를 결정하는데 있어 채널 저항의 영향이 절대적이다. 이에 몇 가지 아크 방전에서의 채널 저항 모델들을 이용하여 특정 전류 파형에서 정전 용량의 변화에 따른 E^* 의 변화를 비교하였다. 그 결과, 채널 저항이 일정한 값일 경우에는 E^* 가 정전 용량이 클수록 같이 증가하는 양상을 보인 반면, 아크 방전 저항 모델들의 경우에는 정전 용량이 클수록 E^* 가 특정 정전 용량 이상에서 거의 일정한 값을 보임을 알 수 있었다. 실제 실험 결과는 아크 방전 저항 모델들의 결과와 유사하였으며, 채널 저항은 시간에 따라 급격히 감소하는 형태를 갖고 있음을 알 수 있었다. 이는 방전 초기 채널 저항의 변화가 채널에 전달되는 파워를 결정하는 중요한 요소임을 방증한다.

그러나 시간에 따른 채널 저항 변화를 명확히 정의하기는 쉽지 않다. 방전 초기 높은 채널 저항에 의해 저항 가열(ohmic heating)이 일어나면 이는 채널 저항을 낮추는 역할을 하며, 낮아진 채널 저항은 다시 채널에 전달되는 파워를 변화시킨다. 따라서 자체 일관적인 (self-consistent) 모델의 개발이 필수적이었고, 개발된 모델을 통해 실험 결과를 검증하여 강한 충격파 발생을 위한 최적의 운전 조건을 제시하고자 하였다.

충격파의 응용을 위해 세가지 운전 변수에 따른 충격파 압력 침투치의 변화를 실험 및 모델을 통해 살펴보았다. 첫 번째 운전 조건인 정전 용량에 대해서는 특정 정전 용량보다 클 때 E^* 가 일정해지는 경향을 보임을 알 수 있었다. 이는 특정 정전 용량 이상에서 방전 초기 파워 파형 및 t^* 가 거의 유사하기 때문이다. 두 번째 운전 조건인 방전 개시 전압에 대해서는 방전 개시 전압을 증가시킬수록 E^* 도 같이 상승하는 것을 알 수 있었다. 이는 방전 개시 전압이 커질수록 t^* 는 일정해지지만 파워 파형이 급격히 증가하기 때문이다. 세 번째 운전 조건인 전극 거리에 대해서는 전극 거리가 멀수록 채널 저항이 높게 유지되기 때문에 저항 가열 파워가 더 높게 유지된다. 따라서 강한 충격파의 압력 침투치를 높이기 위해선 최적의 정전 용량에서 방전 개시 전압과 전극 거리를 증가시키는 것이 효과적임을 알 수 있었다.

주요어 : 수중 펄스 스파크 방전, 충격파, 압력 침투치, 최대 채널 팽창 속도, 가속 구간동안 채널에 전달된 에너지 (E^*), 채널 저항

학번 : 2008-30897